POLYCRYSTALLINE PLASTICITY MODELING OF ANISOTROPIC GRAIN STRUCTURES AND STATISTICAL SIZE EFFECT IN METALLIC ALLOYS

A THESIS SUBMITTED TO
THE GRADUATE SCHOOL OF NATURAL AND APPLIED SCIENCES
OF
MIDDLE EAST TECHNICAL UNIVERSITY

BY

ORHUN BULUT

IN PARTIAL FULFILLMENT OF THE REQUIREMENTS
FOR
THE DEGREE OF MASTER OF SCIENCE
IN
AEROSPACE ENGINEERING

JUNE 2022

Approval of the thesis:

POLYCRYSTALLINE PLASTICITY MODELING OF ANISOTROPIC GRAIN STRUCTURES AND STATISTICAL SIZE EFFECT IN METALLIC ALLOYS

submitted by **ORHUN BULUT** in partial fulfillment of the requirements for the degree of **Master of Science in Aerospace Engineering Department, Middle East Technical University** by,

Prof. Dr. Halil Kalıpçılar
Dean, Graduate School of **Natural and Applied Sciences** _____

Prof. Dr. Serkan Özgen
Head of Department, **Aerospace Engineering** _____

Assoc. Prof. Dr. Tuncay Yalçınkaya
Supervisor, **Aerospace Engineering, METU** _____

Examining Committee Members:

Prof. Dr. Demirkan Çöker
Aerospace Engineering, METU _____

Assoc. Prof. Dr. Tuncay Yalçınkaya
Aerospace Engineering, METU _____

Assoc. Prof. Dr. Hüsnü Dal
Mechanical Engineering, METU _____

Assoc. Prof. Dr. Ercan Gürses
Aerospace Engineering, METU _____

Assoc. Prof. Dr. Cihan Tekoğlu
Mechanical Engineering, TOBB UET _____

Date:14.06.2022

I hereby declare that all information in this document has been obtained and presented in accordance with academic rules and ethical conduct. I also declare that, as required by these rules and conduct, I have fully cited and referenced all material and results that are not original to this work.

Name, Surname: Orhun Bulut

Signature :

ABSTRACT

POLYCRYSTALLINE PLASTICITY MODELING OF ANISOTROPIC GRAIN STRUCTURES AND STATISTICAL SIZE EFFECT IN METALLIC ALLOYS

Bulut, Orhun
M.S., Department of Aerospace Engineering
Supervisor: Assoc. Prof. Dr. Tuncay Yalçınkaya

June 2022, 71 pages

In this thesis, two important microstructural phenomena affecting the plastic behavior of metallic materials are addressed through a local crystal plasticity modeling framework. Initially the influence of anisotropic grain structure developing during various forming procedures and additive manufacturing processes is studied following a multiscale modeling strategy, where Representative Volume Elements (RVEs) are analyzed under axial loading conditions. Macroscopic response of different degrees of anisotropic microstructures and related lattice alignment effects are discussed in detail. Then, the influence of specimen thickness to grain size ratio affecting the forming behavior of micron sized specimens is studied. The statistical size effect that can be captured through a local crystal plasticity model is discussed in comparison to the existing literature. The thesis is concluded with an outlook for possible future studies.

Keywords: Crystal Plasticity, Additive Manufacturing, Anisotropic Microstructure, Texture, Statistical Size Effect

ÖZ

METAL ALAŞIMLARDA ANİZOTROPİK TANE YAPISI VE İSTATİSTİKSEL BOYUT ETKİSİNİN POLİKRİSTAL PLASTİSİTE İLE MODELLENMESİ

Bulut, Orhun
Yüksek Lisans, Havacılık ve Uzay Mühendisliği Bölümü
Tez Yöneticisi: Doç. Dr. Tuncay Yalçınkaya

Haziran 2022 , 71 sayfa

Bu tezde, metalik malzemelerin plastik davranışını etkileyen iki önemli mikroyapısal olay, lokal bir kristal plastisite modelleme çerçevesinde ele alınmaktadır. İlk olarak, çeşitli şekillendirme prosedürleri ve eklemeli imalat süreçleri sırasında gelişen anizotropik tane yapısının etkisi, Temsili Hacim Elemanlarının eksenel yükleme koşulları altında analiz edildiği çok ölçekli bir modelleme stratejisi takip edilerek incelenmiştir. Farklı derecelerde anizotropik olan mikro yapıların makroskopik tepkisi ve buna bağlı tane yönelimi etkileri ayrıntılı olarak tartışılmıştır. Daha sonra, mikron boyutlu numunelerin şekillendirme davranışını etkileyen numune kalınlığının tane boyutuna oranının etkisi incelenmiştir. Lokal bir kristal plastisite modeli aracılığıyla yakalanabilen istatistiksel boyut etkisi, mevcut literatürle karşılaştırmalı olarak tartışılmıştır. Tez, gelecekteki olası çalışmaları da kapsayan bir bakış açısı ile sonuçlandırılmıştır.

Anahtar Kelimeler: Kristal Plastisite, Eklemeli İmalat, Anizotropik Mikroyapı, Doku,

İstatistiksel Boyut Etkisi

To my family...

ACKNOWLEDGMENTS

First of all, I would like to thank to my supervisor Assoc. Prof. Dr. Tuncay Yalçinkaya for his guidance, support, showing great effort to help me finishing my M.Sc. study. He will always serve as a model for me especially his ambition for academy.

I am also thankful to Nazlı Barçın Doğan for her invaluable support. The advice she gave me during hard times was really helpful. I also would like to thank to my friends Mert Ali Andırın and Gökçe Törenli for their friendship.

I would like to thank Sadık Sefa Açar for being a great colleague and Enes Günaydın for his support. I also thank other members of Yalçınkaya Research Group for sharing their ideas during discussions.

Most importantly, I would like to express my deepest thanks to my beloved family. I am grateful to my father Orhan Bulut, my mother Nurdan Bulut and my brother Çağlar Bulut for their encouragement and putting their faith in me.

TABLE OF CONTENTS

ABSTRACT v

ÖZ vi

ACKNOWLEDGMENTS ix

TABLE OF CONTENTS x

LIST OF TABLES xii

LIST OF FIGURES xiii

CHAPTERS

1 INTRODUCTION 1

1.1 Additive Manufacturing 2

1.2 Anisotropic Grain Structures 4

1.3 The Influence of Thickness to Grain Size Ratio 6

1.4 The Outline of the Thesis 8

2 CONSTITUTIVE MODELING 11

2.1 Kinematics of the Crystal Plasticity Model 11

2.2 Formulation of Crystal Plasticity 16

2.3 Slip in Crystals 18

2.4 Grain Orientations in Polycrystalline Materials 19

3 FINITE ELEMENT MODELING 23

3.1 Representative Volume Element (RVE) 23

3.2 Implementation of Boundary Conditions 24

3.2.1 Boundary Conditions for Tensile Specimen Calculations . . . 24

3.2.2 Boundary Conditions for Representative Volume Element Calculations 25

3.3 Homogenization 27

3.4 Parameter Identification 28

3.5 Tensile Specimens 29

3.6 RVE Analyses for Morphological and Orientation Study 32

3.6.1 Crystal orientations for RVE Analyses 32

3.6.2 Aligned Grain Orientations 34

4 RESULTS AND DISCUSSIONS 45

4.1 RVE Analyses 45

4.2 Tensile Specimen Results for t/d Effect 51

5 CONCLUSIONS 59

5.1 RVE Analyses for Anisotropic Grain Structure 59

5.2 t/d Effect on Full Size Micron Specimens 60

REFERENCES 63

LIST OF TABLES

TABLES

Table 2.1 Slip systems for fcc crystals 19

Table 3.1 Dimensions and corresponding t/d ratios of examined specimens. . . 30

Table 3.2 Restricted intervals of RVEs with their corresponding mean resultant angles. 36

Table 3.3 Resultant angles of grains for different RVEs when all the grains having same angle to BD is maintained 40

LIST OF FIGURES

FIGURES

Figure 1.1 Different Additive Manufacturing Methods from [8] 3

Figure 1.2 Schematics of powder bed fusion equipment; (a) Selective laser melting and (b) electron beam melting from [7]. 4

Figure 1.3 3-D optical metallograph image view for a cylindrical component (x-axis) fabricated in argon gas environment from [17]. 5

Figure 1.4 Experimental true stresses for different t/d ratios of nickel at 0.05 and 0.03 strain presented in [33]. 7

Figure 2.1 Kinematic model of elastoplastic deformation [48] 12

Figure 2.2 Pole figure representation with cubes 21

Figure 2.3 Possible cubic orientations for a same point at pole figure 21

Figure 3.1 Virtually created RVE microstructure with 300 grains. 24

Figure 3.2 Boundary conditions for uniaxial tension simulation. 25

Figure 3.3 Location of master node and surfaces on RVE. 26

Figure 3.4 Comparison of stress strain responses of RVEs with fitted parameter and experimental study presented in [64] 28

Figure 3.5 Microstructures of specimens having different t/d values below 1. 29

Figure 3.6 Microstructures of specimens having different t/d values above 1. 31

Figure 3.7 Microstructures of specimens having different t/d values. 32

Figure 3.8 RVEs with different grain morphology; (a) Equiaxed, (b) Needle1, (c) Needle2, (d) Needle3 33

Figure 3.9 Corresponding $\alpha/2$ for the mean angle of rotation for rotation restriction between – α and + α 34

Figure 3.10 Pole figure for [-1 +1] & $0.7°$ MRA. 37

Figure 3.11 Pole figure for [-10 +10] & $7.1°$ MRA. 37

Figure 3.12 Pole figure for [-20 +20] & $14.1°$ MRA. 37

Figure 3.13 Pole figure for [-30 +30] & $21.2°$ MRA. 38

Figure 3.14 Pole figure for [-45 +45] & $31.7°$ MRA. 38

Figure 3.15 Pole figure for [-70 +70] & $49.1°$ MRA. 38

Figure 3.16 Pole figure for [-80 +80] & $56°$ MRA. 39

Figure 3.17 Pole figure for [-90 +90] & $62.8°$ MRA. 39

Figure 3.18 Pole figure for [-110 +110] & $76.2°$ MRA. 39

Figure 3.19 Pole figure for [-130 +130] & $89.3°$ MRA. 40

Figure 3.20 Pole figure for full randomly oriented RVE. 40

Figure 3.21 Pole figure for RVEs with all grains having $5°$ resultant angle. . . 41

Figure 3.22 Pole figure for RVEs with all grains having $10°$ resultant angle. . 41

Figure 3.23 Pole figure for RVEs with all grains having $20°$ resultant angle. . 41

Figure 3.24 Pole figure for RVEs with all grains having $30°$ resultant angle. . 42

Figure 3.25 Pole figure for RVEs with all grains having $50°$ resultant angle. . 42

Figure 3.26 Pole figure for RVEs with all grains having $60°$ resultant angle. . 42

Figure 3.27 Pole figure for RVEs with all grains having $70°$ resultant angle. . 43

Figure 3.28 Pole figure for RVEs with all grains having $80°$ resultant angle. . 43

Figure 3.29 Pole figure for RVEs with all grains having $90°$ resultant angle. . 43

Figure 4.1 Stress versus strain response for different microstructures with random orientations loaded in building and normal directions. 46

Figure 4.2 Stress versus strain response for different microstructures loaded in building (BD) and normal direction (ND). 46

Figure 4.3 Stress versus strain response for microstructures with different morphologies and orientation alignment. 47

Figure 4.4 Von Mises stress distribution for different microstructures loaded in the building direction. 48

Figure 4.5 Von Mises stress distribution for different microstructures loaded in the normal direction. 49

Figure 4.6 Von Mises stress distribution for equiaxed morphology RVEs with different orientation restrictions. 50

Figure 4.7 Stress vs Mean Resultant Angle for RVEs with restricted grain orientations at 10% displacement. 51

Figure 4.8 Stress vs Resultant Angle for RVEs with grains having exact resultant angle at 10% displacement. 51

Figure 4.9 Engineering stress-engineering strain curves for specimens having different t/d ratios at 10% displacement. 52

Figure 4.10 Flow stress values at different strains of specimens having different t/d ratios. 53

Figure 4.11 Von Mises stress distribution of specimens having different t/d ratios below 1 at 10% displacement. 55

Figure 4.12 Von Mises stress distribution of specimens having different t/d ratios above 1 at 10% displacement. 56

Figure 4.13 Von Mises stress distribution of specimens having different t/d ratios at 10% displacement. 57

CHAPTER 1

INTRODUCTION

Even though the usage of light and strong materials such as composites is increasing day by day in aerospace industry, the metallic materials still dominate the field due to their various advantages. After the recent developments in metal additive manufacturing, it is now possible to design and manufacture lighter and strong metallic components. However, the fatigue and ductile behavior performance of these materials is quite problematic due to their microstructure which might include serious porosity and anisotropic grain structure (see e.g. [1], [2]). The microstructure is process dependent and quite difficult to control, leading to a scatter in the macroscopic response. Therefore, it is crucial to study the developing microstructure in order to understand the macroscopic behavior which could only be done following a methodology at the grain or lower scales. The crystal plasticity framework is a good candidate in this context which can capture the anisotropic behavior but still feasible to use for macroscopic understanding.

The main interest in this work concentrates on the anisotropic grain growth observed during the additive manufacturing processes (see e.g. [3]). The grain structure and the lattice orientation align itself in the building direction of the process, which indeed results in a texture. The influence of both the morphology and the texture should be analyzed in detail. Therefore, the effect of different grain morphologies and lattice orientation alignment on the plastic response of the materials is studied following a computational multi-scale approach. The polycrystalline representative volume element microstructures are generated through Voroni tessellation including different alignment scenarios. The outcome is discussed at the homogenized macroscopic constitutive response level and the spatial stress evolution at the micro scale.

The other phenomenon investigated in this thesis is the influence of the thickness to grain size ratio during micro forming operations. This is a statistical size effect which should be separated from the intrinsic Hall-Petch effect. Relative size of thickness to average grain size of the material has important influence on the mechanical behavior (see e.g. [4]). When fewer grains exist along the thickness direction, mechanical behavior of the specimens differ from the bulk specimen (see e.g. [5], [6]). The experimentally observed phenomenon is studied through a local crystal plasticity framework here in order to focus solely on the statistical effect. The capacity of the modeling strategy is discussed and possible improvements are proposed.

1.1 Additive Manufacturing

Additive manufacturing of metallic alloys has become quite popular for the over 30 years with the development of new AM techniques which provide a number of major advantages, including a wide range of geometric capabilities, a low necessity for human engagement, and a shorter design cycle time. The employment of this process in aerospace industry is crucial and requires enormous effort both in process itself and heat treatment. Aircraft engine components, vehicle parts, and space components have adopted functional AM parts with complex geometries (see e.g. [7]). Different methods and their categorization are shown in Figure 1.1.

Powder bed fusion, direct energy deposition, metal binder jetting, and sheet lamination are four of AM techniques which are commonly used (see e.g. [9], [10]). Among these techniques, powder bed fusion (PBF) is the most popular AM process (see e.g. [11]). PBF is separated into two main techniques based on the kind of power source: selective laser melting (SLM), which employs a high-intensity laser, and electron beam melting (EBM), which uses an electron beam. Both techniques require the use of a powder-holding platform. Even though the working principles of these two processes are similar, the processing steps are quite different [12]. The schematics of the SLM and EBM setups are shown in Figure 1.2. In the SLM process, the laser beam passes through a set of lenses and is reflected by a mirror onto the platform surface in the SLM process. The mirrors are used to regulate the laser beam spot movement on the predefined paths in the planar (X and Y) directions. The platform travels lower

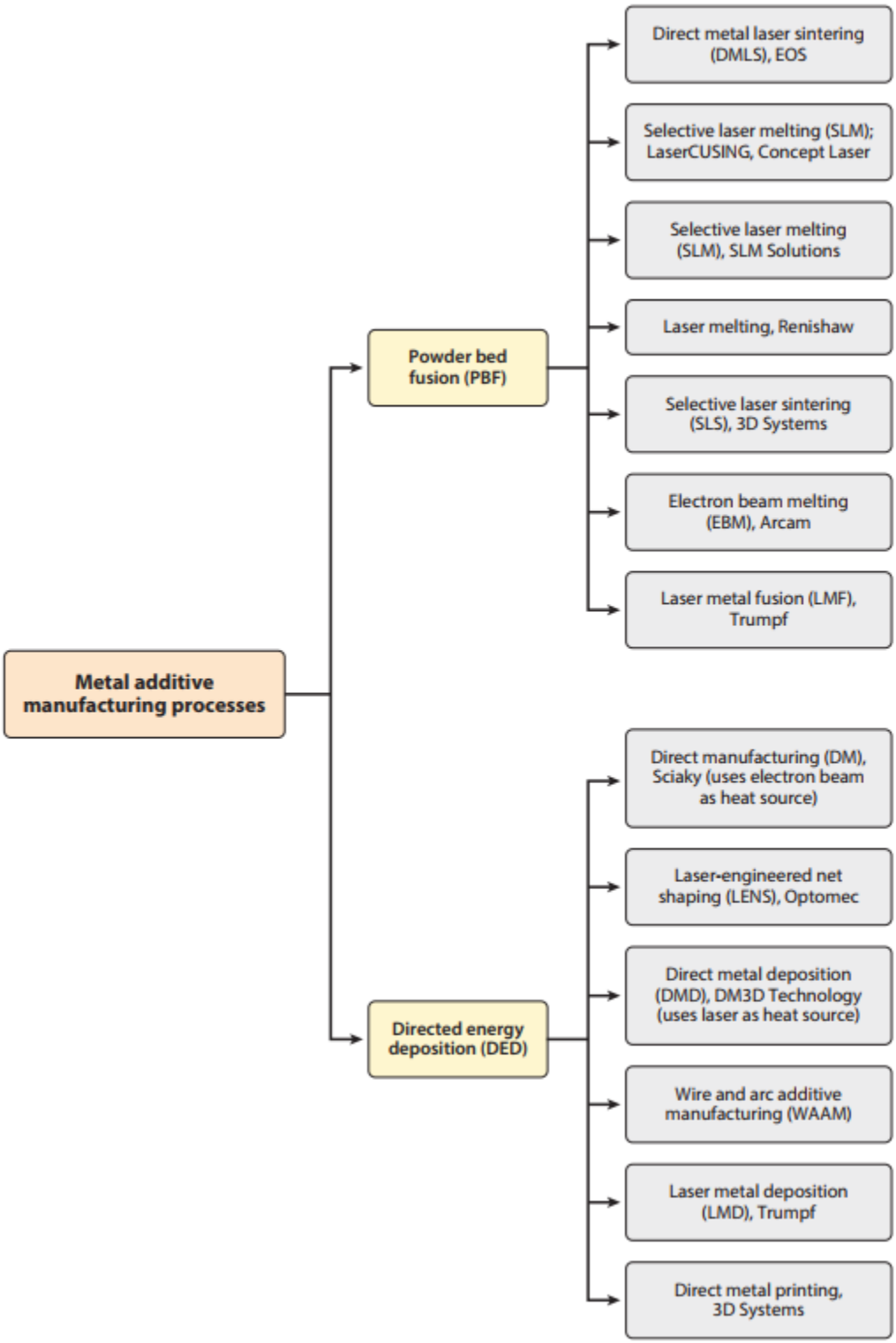

Figure 1.1: Different Additive Manufacturing Methods from [8]

after a layer of powder is selectively melted, and a recoating blade or brush pushes another layer of fresh powder from the powder tank to the top of the previously constructed surface, repeating the laser scan process. To prevent oxidation of metallic powders at high temperatures, the construction chamber of an SLM machine is filled with an inert gas, usually argon. The scanning electron microscope (SEM) method was used to develop the EBM process. It utilizes a much higher-power electron beam to selectively melt the powder. The EBM procedure needs a vacuum environment. The electron beam source is positioned on top of the powder bed, as indicated in Figure 1.2. A lens mechanism controls the movement of the electron beam directly. A powder hopper delivers fresh powder onto the platform's side, and a rake coats a layer of powder on top of the previously melted layer (see e.g. [13], [14]).

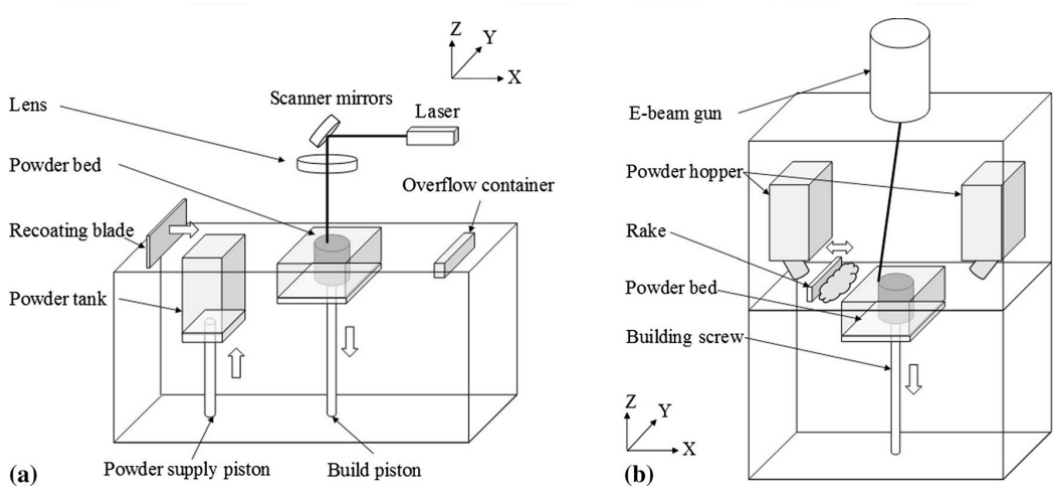

Figure 1.2: Schematics of powder bed fusion equipment; (a) Selective laser melting and (b) electron beam melting from [7].

1.2 Anisotropic Grain Structures

Understanding the evolution of microstructure and crystallographic texture throughout manufacturing processes is critical because grain size, shape, and texture have a significant impact on the mechanical performance of the final product. Grain shapes that deviate from equiaxed morphology have been observed in industrial applications of forming techniques, particularly in additive manufacturing. It is well understood that the mechanical characteristics and the development of these distinctive mor-

phologies are associated. Due to thermal and mechanical factors, grains are found to be elongated in particular orientations during manufacturing operations. Example of an elongated grain structure can be seen in Figure 1.3. An anisotropic, direction-sensitive response is obtained when grains are aligned in a specific direction (see e.g. [7, 15, 16, 17]).

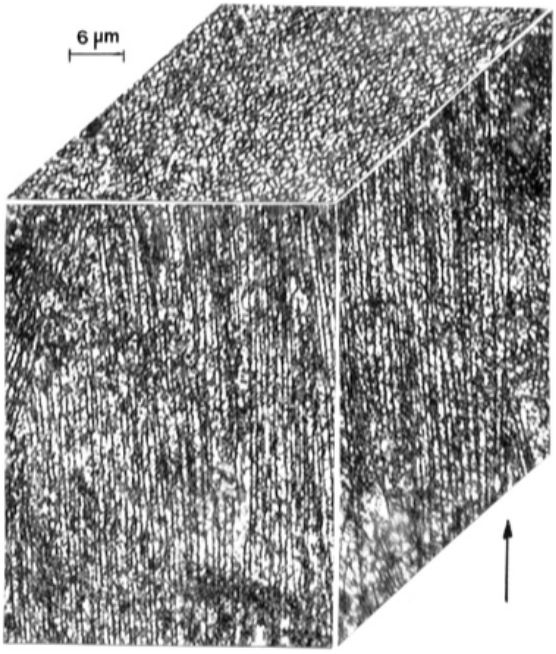

Figure 1.3: 3-D optical metallograph image view for a cylindrical component (x-axis) fabricated in argon gas environment from [17].

Anisotropic and heterogeneous microstructures as well as preferential crystal orientations are observed for additive manufacturing applications such as Powder-Bed Fusion (PBF) and Directed Energy Deposition (DED) techniques (see e.g. [16]). Products of additive manufacturing have grains elongated in the direction along the highest temperature gradient during rapid solidification, resulting in columnar grains (see e.g. [18], [19]). The morphology and the orientation of the additively manufactured microstructures are determined by material properties and process parameters such as scan velocity, laser or beam power, scan strategy and hatch spacing (scan spacing). With the pursuit of optimum mechanical properties, different process parameters have been tested for years. Grain morphologies and crystallographic orientations resulting from the experiments have been analyzed (see e.g. [20], [21], [22]). Examining

the additively manufactured products reveals that emergence of the columnar grain structure is often accompanied by the crystal orientation alignment (see e.g. [23]). Moreover, orientations of the grains are related to the proportion of the elongation (i.e. aspect ratio) of grains. In some cases, the grains are so elongated that they start to be called "fibers" whereas, in some other cases, the grain aspect ratio is not that extreme (see e.g. [24]). Consequently, crystal orientations vary from case to case depending upon the morphology. Corresponding aligned structure results in plastic anisotropy. In the literature, the combined effect of orientation and morphology resulted in a weaker stress response along the direction in which the crystallographic structure is oriented (see e.g. [24], [25]). In terms of yield and flow stress experiments have shown that materials are weaker in the direction they are textured (see e.g. [26], [27], [28]).

Various experimental studies addressed the crystal structure of additively manufactured products. However, it is not possible to conduct a controlled study where the microstructure is designed during the process to examine its influence. Yet it is possible to make such a study using computational techniques.

1.3 The Influence of Thickness to Grain Size Ratio

Micron-sized devices are becoming increasingly important in numerous sectors as a result of continuous technological breakthroughs. Because of the growing popularity of such tiny devices, further research into the impact of microstructural features on mechanical response is required. At this length scale, different size effect phenomena play crucial role in the plastic behavior of the materials (see e.g. [29]). As the material become thinner, fewer grains are present along the thickness direction. Hall-Petch relation dictates that material strength strongly depends on the grain size with an inverse relation, which assumes a certain dependency for every grain size independent of the specimen geometry (see [30]). However, this relation is not always sufficient to explain the mechanical behavior of materials. There are some cases, where the changes in mechanical behaviors are cannot simply be explained by Hall-Petch relation like cases with thin specimens (see e.g. [31, 32]).

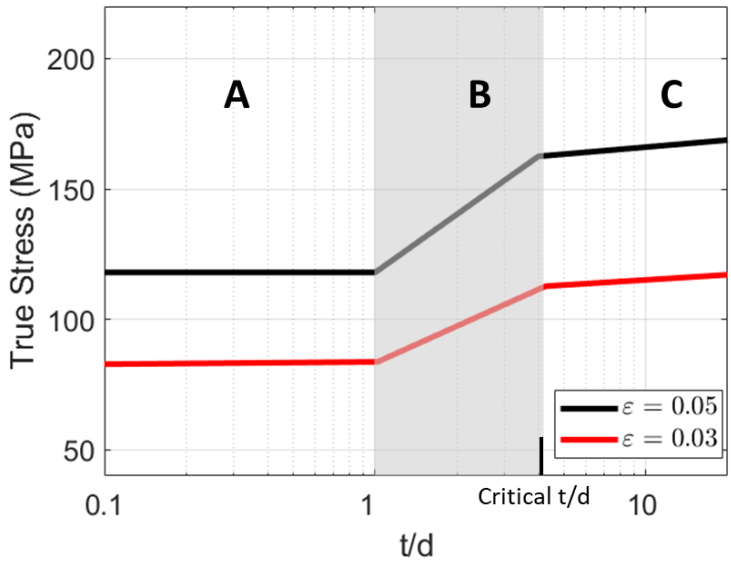

Figure 1.4: Experimental true stresses for different t/d ratios of nickel at 0.05 and 0.03 strain presented in [33].

There have been various experimental studies which have investigated the effect of thickness to grain size ratio in the literature. These experimental studies have shown that thickness to grain size ratio (t/d) is a significant factor on the account of mechanical behavior (see e.g. [31, 33, 34]). The thickness to grain size ratio (t/d) is controlled in these experiments by either keeping the thickness constant while altering the grain size (by heat treatment) or retaining the same grain size for varying thickness values. Variation in mechanical responses is observed among these specimens. Flow stress decreases with decreasing thickness to grain size ratio (t/d) much more drastically for thin specimens in a certain interval. Therefore, in this interval, thin materials follow a different trend from the bulk specimens in terms of flow stress and show a "multicrystalline behavior", see region B in Figure 1.4. The value of t/d below which specimens follow this trend, is called critical value. The critical value differs for each material. After that critical value, material behave like a "polycrystal", see region C in in Figure 1.4.Moreover, for specimens having less than one grain per thickness which is called "monocrystals", similar values of flow stress are recorded, see region A in Figure 1.4. This is due to the fact that surface grain ratio stays constant for all specimens, since all the grains are surface grains.

As fewer grains are present along the thickness direction, the ratio of grains having at least one free surface increases. Therefore, surface grains become more and more dominant on the specimen which leads to inferior mechanical properties (see e.g. [5]). The main reason is that the inner grains are much more constrained by the neighboring grains than surface grains leading to more dislocation grain boundary interaction and more hardening. The exponential decrease of flow stress with the decrease of t/d is explained by this proportional increase of free surface (see e.g. [31], [35], [36], [37]). Moreover, low t/d ratio might lead to an anisotropic behavior since each grain will possess a strong influence on the overall behavior. Besides anisotropy, the grain boundaries (GBs) are also crucial in these specimens which can be grouped as vertical GB (along thickness direction) and horizontal GB (along the loading direction). For t/d values below 1, only vertical GBs are present since all grains become columnar. However, for t/d values higher than 1, grains start to stack on each other and horizontal GBs come into action. As the t/d is further increased until the critical value, the amount of the horizontal grain boundaries increases significantly, which can be regarded as one of the factors that ensures the increase in flow stress in the interval before the critical value (see e.g. [31], [33]).

A framework for studying the effect of thickness to grain size ratio with crystal plasticity is established and presented in [38]. A local crystal plasticity model is employed to assess the mechanical behavior of thin materials. Specimens with varying t/d ratios are created and subjected to the uniaxial tensile loading simulations. The obtained results are compared with experimental studies and the capacity of crystal plasticity finite element calculations is discussed in this context.

1.4 The Outline of the Thesis

The layout of the thesis is as follows. In Chapter 2 the local crystal plasticity theory used in this thesis is explained where the slip systems in the crystals are addressed as well. Grain orientation in polycrystalline materials with their pole figure representations is also presented. In Chapter 3, crystal finite element modeling and given boundary conditions for both tensile specimens and representative volume elements (RVEs) are explained. The homogenization and the parameter identification proce-

dures discussed. Pole figures of the analyzed RVEs are presented. In Chapter 4, the numerical results of both tensile specimens and RVEs are discussed. Finally, in Chapter 5 conclusions and outlook are presented.

CHAPTER 2

CONSTITUTIVE MODELING

In this chapter, the formulation of the crystal plasticity framework is explained in detail. First, the kinematics of finite deformation is introduced. Then crystal plasticity theory and the stress update methodology are addressed. All the simulations are performed with the commercial finite element analysis software ABAQUS. A user material subroutine (UMAT) is modified and used to predict the plastic behavior of the polycrystal (see [39]). The slip systems of crystalline materials is presented and the grain orientations in polycrystalline materials and pole figures are explained.

2.1 Kinematics of the Crystal Plasticity Model

The kinematical theory describing the crystal behavior proposed by Taylor [40] and later turned into a precise mathematical theory by Hill and Rice [41, 42, 43] is used in the formulation of the crystal plasticity theory. The key equations of this theory, based on the works of Rice [44] and Asaro [45], is summarized in this section.

Metals are crystalline materials, so their individual atoms are grouped into a periodic, repeating shape known as a crystal. Elastic deformation is defined as the stretching of interatomic bonds between atoms, and plastic deformation (slip) is defined as the breaking and re-forming of bonds when one plane of atoms moves relative to another (see e.g. [46, 47]).

The crystalline material is allowed to flow through the lattice through dislocation motion, hence, crystalline slip. The lattice, on the other hand, is allowed to go through elastic deformations. This way, the inelastic deformation of the crystal rises from

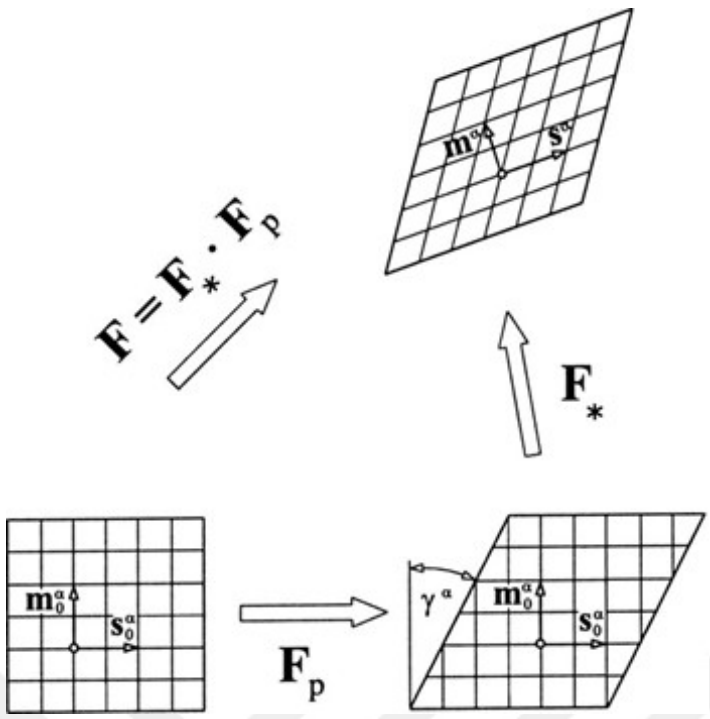

Figure 2.1: Kinematic model of elastoplastic deformation [48]

crystalline slip, which does not distort the crystal lattice, as seen in 2.1.

The deformation gradient, mapping the reference configuration of the material to the spatial configuration, can be decomposed as

$$\mathbf{F} = \mathbf{F}^* \cdot \mathbf{F}^p \tag{2.1}$$

where $\mathbf{F}^*$ describes the elastic stretching and rotation of the lattice, decomposed as

$$\mathbf{F}^* = \mathbf{F}^e \cdot \mathbf{F}^R \tag{2.2}$$

where $\mathbf{F}^e$ and $\mathbf{F}^R$ correspond to elastic stretching and rotation of the lattice, respectively. $\mathbf{F}^p$ describes the plastic shear of the material, i.e., the permanent deformation, at an intermediate configuration where lattice orientation and stretching are the same as reference configuration. For a single crystal with a single slip system, $\mathbf{F}^p$ can be written as

$$\mathbf{F}^p = 1 + \gamma \mathbf{s} \otimes \mathbf{m} \tag{2.3}$$

where $\mathbf{s}$ and $\mathbf{m}$ are slip directions and normal to slip plane, respectively. γ is the total plastic slip. In the case of presence of multiple slip systems, the rate of change $\mathbf{F}^p$ is described as

$$\dot{\mathbf{F}}^p \cdot (\mathbf{F}^p)^{-1} = \sum_{\alpha=1}^{N} \dot{\gamma}^{(\alpha)} (\mathbf{m}^{(\alpha)} \otimes \mathbf{s}^{(\alpha)}) \tag{2.4}$$

where $\dot{\gamma}^{(\alpha)}$ is the slip rate of an individual slip system α. The slip direction and normal to the slip planes in the deformed configuration are defined as

$$\begin{aligned} \mathbf{s}^{*^{(\alpha)}} &= \mathbf{F}^* \cdot \mathbf{s}^{(\alpha)} \\ \mathbf{m}^{*^{(\alpha)}} &= \mathbf{m}^{(\alpha)} \cdot \mathbf{F}^{*^{-1}} \end{aligned} \tag{2.5}$$

Using the decomposed components of deformation gradient, the velocity gradient L can be obtained in terms of $\mathbf{F}^*$ and $\mathbf{F}^p$ as

$$\mathbf{L} = \dot{\mathbf{F}}\mathbf{F}^{-1} = (\dot{\mathbf{F}^*\mathbf{F}^p})(\mathbf{F}^*\mathbf{F}^p)^{-1} \tag{2.6}$$

It can be rewritten as

$$(\dot{\mathbf{F}^*\mathbf{F}^p})(\mathbf{F}^*\mathbf{F}^p)^{-1} = \dot{\mathbf{F}}^*\mathbf{F}^{*^{-1}} + \mathbf{F}^*\dot{\mathbf{F}}^p(\mathbf{F}^*\mathbf{F}^p)^{-1} \tag{2.7}$$

This results in components of the velocity gradient corresponding to lattice deformation and plastic slip, $\mathbf{L}^*$ and $\mathbf{L}^p$ respectively.

$$\begin{aligned} \mathbf{L}^* &= \dot{\mathbf{F}}^*\mathbf{F}^{*^{-1}} \\ \mathbf{L}^p &= \mathbf{F}^*\dot{\mathbf{F}}^p(\mathbf{F}^*\mathbf{F}^p)^{-1} = \mathbf{F}^*\dot{\mathbf{F}}^p\mathbf{F}^{p^{-1}}\mathbf{F}^{*^{-1}} \end{aligned} \tag{2.8}$$

Inserting the rate of $\mathbf{F}^p$ here, one can find

$$\mathbf{L}^p = \mathbf{F}^*\dot{\mathbf{F}}^p\mathbf{F}^{p^{-1}}\mathbf{F}^{*^{-1}} = \sum_{\alpha=1}^{N} \dot{\gamma}^{(\alpha)}(\mathbf{m}^{(\alpha)} \otimes \mathbf{n}^{(\alpha)}) \tag{2.9}$$

Additionally, the velocity gradient can be decomposed into symmetric and skew-symmetric parts describing rate of stretching and spin.

$$\begin{aligned} \mathbf{L}_{sym} =& \mathbf{D}^* + \mathbf{D}^p \\ \mathbf{L}_{skew} =& \mathbf{\Omega}^* + \mathbf{\Omega}^p \end{aligned} \tag{2.10}$$

where $\mathbf{D}$ is symmetric rate of stretching and $\mathbf{\Omega}$ is antisymmetric spin tensor. Thus, we have defined the kinematics of crystal behavior. Before defining the constitutive laws governing crystal plasticity, it is necessary to introduce objective stress rates.

The rate definition of stress tensors requires material objectivity, i.e., invariance with the material frame. While this condition is always satisfied for stress and strain measures of reference configurations, objectivity is not guaranteed for stress and strain measures of spatial configuration [49]. One of the commonly used stress rate definitions in continuum mechanics is Jaumann stress rate, which is used in the implementation of the UMAT subroutine used in this study.

Jaumann stress rate of Cauchy stress tensor σ is defined as

$$\overset{\nabla}{\sigma} = \dot{\sigma} - \mathbf{\Omega}\sigma + \sigma\mathbf{\Omega} \tag{2.11}$$

where $\overset{\nabla}{\sigma}$ is a corotational stress rate on axes rotating with the material. According to Hill and Rice [43], the existence of an elastic potential yields the following relation between symmetric rate of stretching of lattice and Jaumann rate of Cauchy stress tensor, as

$$\overset{\nabla^*}{\sigma} + \sigma(\mathbf{I} : \mathbf{D}^*) = \mathbf{C} : \mathbf{D}^* \tag{2.12}$$

where $\mathbf{I}$ is the second order identity tensor, $\mathbf{C}$ is the tensor of elastic moduli and $\overset{\nabla^*}{\sigma}$ is a corotational stress rate on axes that rotate with crystal lattice, related to corotational stress rate on axes rotating with the material $\overset{\nabla}{\sigma}$ through the following equation

$$\overset{\nabla^*}{\sigma} = \overset{\nabla}{\sigma} + (\mathbf{\Omega} - \mathbf{\Omega}^*) \cdot \sigma - \sigma \cdot (\mathbf{\Omega} - \mathbf{\Omega}^*) \tag{2.13}$$

The crystalline slip obeys Schmid's law, meaning that slipping rate of a slip system $\dot{\gamma}^{(\alpha)}$ depends on the current Cauchy stress σ through a stress called Schmid stress $\tau^{(\alpha)}$. Schmid stress is the resolved shear stress when elastic distortions are negligible. The version based on Rice's [42] thermodynamic stress conjugate to slip is defined as

$$\tau^{(\alpha)} = \mathbf{m}^{*^{(\alpha)}} \cdot \frac{\rho_0}{\rho} \sigma \cdot \mathbf{s}^{*^{(\alpha)}} \tag{2.14}$$

where ρ_0 and ρ are mass densities in reference and spatial configurations. The rate of change of Schmid stress is given as in [43]

$$\dot{\tau}^{(\alpha)} = \mathbf{m}^{*^{(\alpha)}} \cdot [\overset{\nabla^*}{\sigma} + \sigma(\mathbf{I} : \mathbf{D}^*) - \mathbf{D}^* \cdot \sigma + \sigma \cdot \mathbf{D}^*] \cdot \mathbf{s}^{*^{(\alpha)}} \tag{2.15}$$

In rate dependent plasticity, the rate of shear strain of a single crystal is determined with the resolved shear stress as in [50]

$$\dot{\gamma}^{(\alpha)} = \dot{\gamma}_0 \left| \frac{\tau^{(\alpha)}}{g^{(\alpha)}} \right|^n \operatorname{sign}(\tau^{(\alpha)}). \tag{2.16}$$

where $\dot{\gamma}_0$ is the reference strain rate on a slip system, $g^{(\alpha)}$ is the current strength of the slip system from previous plastic strains, $\operatorname{sign}(\tau^{(\alpha)})$ is a function returning the sign of resolved shear stress, and n is the rate sensitivity exponent. The strain hardening of a slip system is characterized by the following equation describing the evolution of strength of each slip system in an incremental manner

$$\dot{g}^{(\alpha)} = \sum_{\beta} h^{\alpha\beta} \left| \dot{\gamma}^{\beta} \right| \tag{2.17}$$

where $h^{\alpha\beta}$ are the slip hardening moduli ranging over all slip systems. In the case of $\alpha = \beta$, self-hardening moduli is represented, and in the case of $\alpha \neq \beta$, latent hardening moduli are represented. The self hardening formulation in the code used in this work is characterized as hyper-secant hardening law [45, 51]

$$h^{\alpha\alpha} = h(\gamma) = h_0 \text{sech}^2 \left| \frac{h_0 \gamma}{g_s - g_0} \right| \tag{2.18}$$

where h_0 is the initial hardening modulus, g_0 and g_s initial and saturation slip resistances of the slip system, and γ is the cumulative shear strain on all slip systems. The cumulative shear strain is described as

$$\gamma = \sum_{\alpha} \int_0^t \left| \dot{\gamma}^{(\alpha)} \right| \ dt \tag{2.19}$$

For latent hardening expression

$$h^{\alpha\beta} = q^{\alpha\beta} h^{\alpha\alpha} \ , \quad (\alpha \neq \beta) \tag{2.20}$$

where $q^{\alpha\beta}$ denotes the ratio of latent hardening to self-hardening.

2.2 Formulation of Crystal Plasticity

In this section, the implementation of crystal-plasticity theory through incremental formulation is explained shortly. Due to material and geometric nonlinearity, it is necessary to use an iterative approach in its implementation. Tangent modulus method for a rate dependent solid is used to determine the increment of plastic shear of a slip system for a time increment Δt as

$$\Delta\gamma^{(\alpha)} = \Delta t \left[(1-\theta)\dot{\gamma}_t^{(\alpha)} + \theta \dot{\gamma}_{t+\Delta t}^{(\alpha)} \right] \tag{2.21}$$

where θ is an integration constant ranging from 0 to 1 corresponding to implicit or explicit Euler integration scheme. Since slipping rate $\dot{\gamma}^{(\alpha)}$ is a function of resolved shear stress (τ) and the current strenght (g), the Taylor expansion of it gives

$$\dot{\gamma}_{t+\Delta t}^{(\alpha)} = \dot{\gamma}_t^{(\alpha)} + \frac{\partial \dot{\gamma}^{(\alpha)}}{\partial \tau^{(\alpha)}} \Delta\tau^{(\alpha)} + \frac{\partial \dot{\gamma}^{(\alpha)}}{\partial g^{(\alpha)}} \Delta g^{(\alpha)} \tag{2.22}$$

where $\Delta\tau^{(\alpha)}$ and $\Delta g^{(\alpha)}$ are increments of resolved shear stress and current strength of the slip system for a time increment Δt, respectively. The incremental relation for the slipping rate of a slip system can then be obtained as

$$\Delta\gamma^{(\alpha)} = \Delta t \left[\dot{\gamma}_t^{(\alpha)} + \theta \frac{\partial \dot{\gamma}^{(\alpha)}}{\partial \tau^{(\alpha)}} \Delta\tau^{(\alpha)} + \theta \frac{\partial \dot{\gamma}^{(\alpha)}}{\partial g^{(\alpha)}} \Delta g^{(\alpha)} \right] \tag{2.23}$$

The incremental formulation of the current strength is

$$\Delta g^{(\alpha)} = \sum_{\beta} h^{\alpha\beta} \Delta\gamma^{(\beta)} \tag{2.24}$$

and the increment of resolved shear stress is

$$\Delta\tau^{(\alpha)} = \left[C_{ijkl}\mu_{kl}^{(\alpha)} + \omega_{ik}^{(\alpha)}\sigma_{jk} + \omega_{jk}^{(\alpha)}\sigma_{ik} \right] \cdot \left[\Delta\varepsilon_{ij} - \sum_{\beta} \mu_{ij}^{(\beta)} \Delta\gamma^{(\beta)} \right] \tag{2.25}$$

where C is the elastic moduli matrix, μ and ω are Schmid factors defined in terms of slip directions and slip plane normals as

$$\mu_{ij}^{(\alpha)} = \frac{1}{2} \left[s_i^{*(\alpha)} m_j^{*(\alpha)} + s_j^{*(\alpha)} m_i^{*(\alpha)} \right] \tag{2.26}$$

$$\omega_{ij}^{(\alpha)} = \frac{1}{2} \left[s_i^{*(\alpha)} m_j^{*(\alpha)} - s_j^{*(\alpha)} m_i^{*(\alpha)} \right] \tag{2.27}$$

Substituting the incremental formulations of resolved shear stress and current strength, we obtain

$$\begin{aligned} &\dot{\gamma}_t^{(\alpha)} \Delta t + \theta \Delta t \frac{\partial \dot{\gamma}^{(\alpha)}}{\partial \tau^{(\alpha)}} \left[C_{ijkl}\mu_{kl}^{(\alpha)} + \omega_{kl}^{(\alpha)}\sigma_{jk} + \omega_{jk}^{(\alpha)}\sigma_{ik} \right] \Delta\varepsilon_{ij} \\ &= \sum_{\beta} \left\{ \delta_{\alpha\beta} + \theta \Delta t \frac{\partial \dot{\gamma}^{(\alpha)}}{\partial \tau^{(\alpha)}} \left[C_{ijkl}\mu_{kl}^{(\alpha)} + \omega_{kl}^{(\alpha)}\sigma_{jk} + \omega_{jk}^{(\alpha)}\sigma_{ik} \right] \mu_{ij}^{\beta} \right. \\ &\qquad \left. - \theta \Delta t \frac{\partial \dot{\gamma}^{(\alpha)}}{\partial g^{(\alpha)}} h_{\alpha\beta} sign(\dot{\gamma}_t^{(\beta)}) \right\} \Delta\gamma^{(\beta)} \end{aligned} \tag{2.28}$$

The rate quantities up until this point are formed on the rotating lattice frame. The UMAT subroutine takes the known current and resolved shear stresses of each slip system, strain and strain increment, and current grain orientation at time t to predict the shear strain increment $\Delta\gamma$. The Newton-Raphson iterative scheme is applied until the convergence is reached according to the following residual equation

$$\Delta\gamma^{(\alpha)} - (1-\theta)\Delta t\dot{\gamma}_t^{(\alpha)} - \theta\Delta t\dot{\gamma}_{t+\Delta t}^{(\alpha)} \leq \epsilon \tag{2.29}$$

Through a Newton-Raphson iteration algorithm, $\Delta\gamma$ is iterated until the convergence criteria is reached, with a tolerance ϵ taken as $10^{(-5)}$ in this work. After this convergence is achieved, the lattice rotations are applied through the following equations as

$$\Delta s_i^{*(\alpha)} = \left\{ \Delta\varepsilon_{ij} + \Omega_{ij}\Delta t - \sum_{\beta} \left[\mu_{ij}^{(\beta)} + \omega_{ij}^{(\beta)} \right] \Delta\gamma^{(\beta)} \right\} s_j^{*(\alpha)} \tag{2.30}$$

$$\Delta m_i^{*(\alpha)} = -m_j^{*(\alpha)} \left\{ \Delta\varepsilon_{ji} + \Omega_{ji}\Delta t - \sum_{\beta} \left[\mu_{ji}^{(\beta)} + \omega_{ji}^{(\beta)} \right] \Delta\gamma^{(\beta)} \right\} \tag{2.31}$$

2.3 Slip in Crystals

The smallest and the most basic periodic part of a crystal lattice is called unit cell. There are 14 different unit cells. For metals, face-centered cubic (FCC), body-centered cubic (BCC), and hexagonal close-packed (HCP) are most commonly observed unit cells. FCC and BCC unit cells are cubic and have cubic symmetry. FCC unit cell consists of 8 one-eight atom, one at each corner and 6 half atom, one at each face center.

The driving force of plastic deformation in crystalline materials are slip systems. Slip systems are crystallographic planes where dislocation motion occurs in a direction on the plane. Thus, they are made of slip normals and slip directions. Different crystal structures have different slip systems. In Schmid plasticity, the resolved shear stress of a slip system is determined by the orientation of its slip normal and slip direction

to the loading direction. It should be noted that plastic deformation cannot always be seen in all slip systems, hence, they are not always active. For example, while BCC crystals can consist of up to 48 slip planes, depending on the temperature of the material, it is possible that only 12 of them show activity.

In this work, we are concerned with the deformation of crystalline materials with face centered cubic (FCC) structure. FCC materials consist of 12 slip systems that can be seen using Miller index notation in Table 2.1, which are all permutations of the slip plane $\{111\}$ and direction <110>. In this rate dependent crystal plasticity framework, they are always considered to be active.

Table 2.1: Slip systems for fcc crystals

Slip Systems	Plane	Direction	Slip Systems	Plane	Direction
1	(111)	$[\bar{1}01]$	7	$(\bar{1}11)$	[101]
2	(111)	$[\bar{1}10]$	8	$(\bar{1}11)$	[110]
3	(111)	$[0\bar{1}1]$	9	$(\bar{1}11)$	$[0\bar{1}1]$
4	$(\bar{1}\bar{1}1)$	[011]	10	$(1\bar{1}1)$	[011]
5	$(\bar{1}\bar{1}1)$	$[\bar{1}10]$	11	$(1\bar{1}1)$	[110]
6	$(\bar{1}\bar{1}1)$	[101]	12	$(1\bar{1}1)$	$[\bar{1}01]$

2.4 Grain Orientations in Polycrystalline Materials

Polycrystalline material consist of many crystals seperated by grain boundaries. During crystallization, grains nucleate at different positions with initial random arrangment of atoms and grow to form grain boundaries with each other, building the polycrstalline structure. In polycrstals, each crystal has a uniform periodic arrangment of atoms through the grain which is called crystal lattice. But the same periodic arrangement does not repeat itself throughout material since crystals may have different crystal orientations. Grains have unique crystal orientation with respect to their neighbours which enables to distinguish a region as a grain (see [52]).

Orientation of a crystal can be assigned with different methods. Commonly used methods in the literature are using Euler angles, Rodrigues vectors, Caley-Klein pa-

rameters and Quaternions. Rotations are used to obtain transformation between crystal's local coordinate system and global coordinate system of the specimen (see [53]).

Crystal orientation of a FCC crystal can be represented by three pole figures. Each pole figure represents the orientation of a plane normal of unit cell of crystal. The plane normals are expressed in terms of Miller indices and must not be parallel to each other. Two plane normals contain required information about the orientation of an object in three dimensional space but for pole figures of crystal orientations, third pole figure is required due to antipodal symmetry.

For FCC crystals, the Miller indices of pole figures are generally determined as (001), (011) and (111) or permutations of these types. A pole figure is drawn by following the procedure such that firstly, a unit cell with a certain orientation is placed at the center of a hemisphere, then the direction vector on the unit cell for which the pole figure is drawn, is continued until it intersects the hemisphere. The procedure is followed for all the grains to obtain intersection points. Finally, the hemisphere is projected onto a plane with equal-area method, and projection points are utilized to draw density map. For instance, In (010) pole figure is shown in Figure 2.2 , each cubic corresponds to a crystal. At the perimeter of the circle, local (010) directions of cubics are perpendicular to normal of the specimen cross-section which is Z axis for this example. That direction is parallel to the normal of the specimen cross-section at the center. A similar relation is observed for (011) pole figure.

Explained phenomena that an orientation is required to be represented by three pole figures is presented visually in Figure 2.3. There are more than one possible orientations located at the same point at a pole figure. Because, when the unit cell is rotated about the pole figure direction, local (010) direction in this case, it's position at the pole figure does not change.

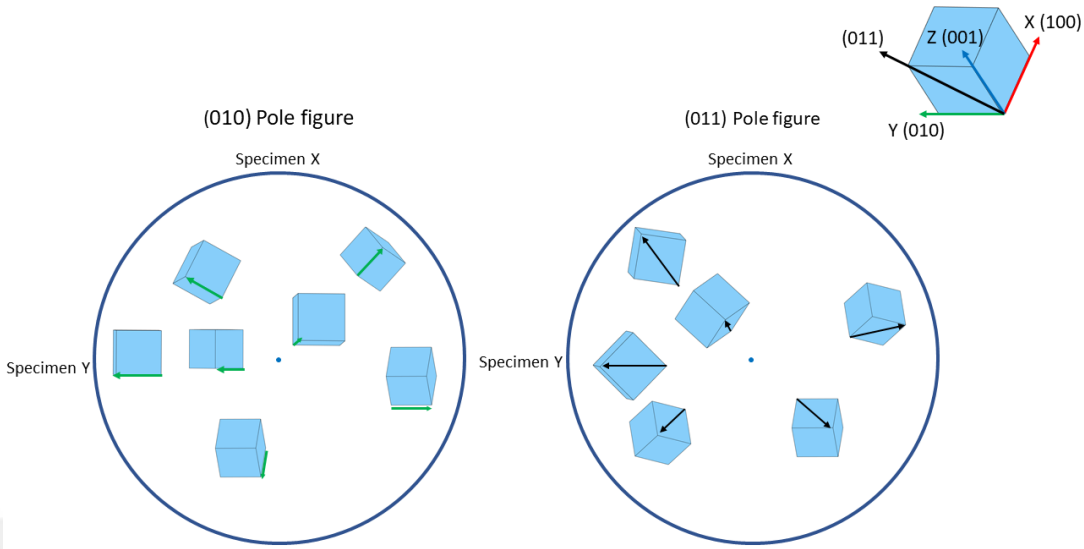

Figure 2.2: Pole figure representation with cubes

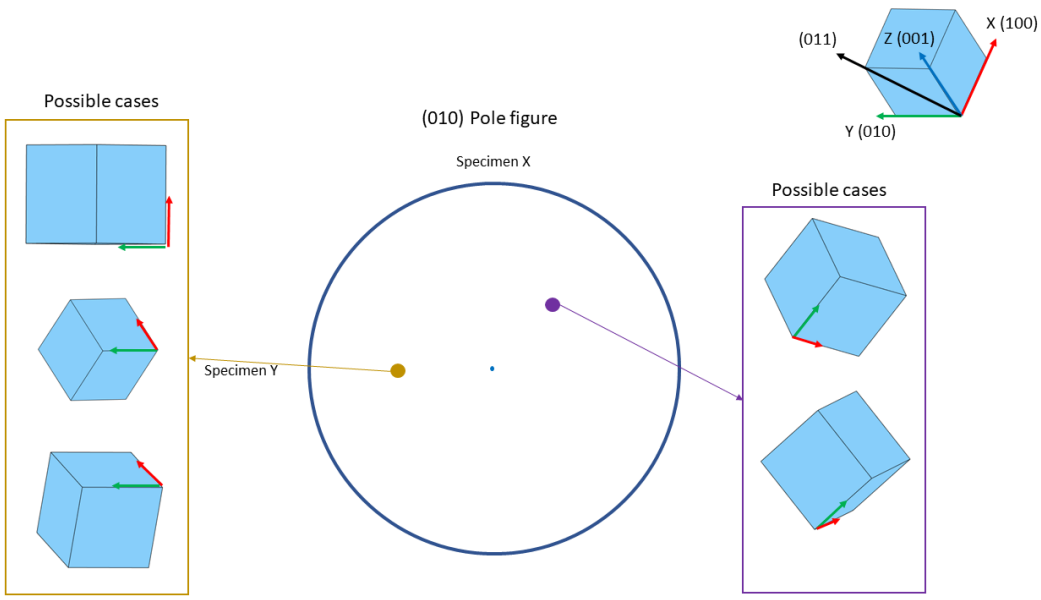

Figure 2.3: Possible cubic orientations for a same point at pole figure

CHAPTER 3

FINITE ELEMENT MODELING

In this chapter, FE (Finite Element) analyses of aforementioned cases are introduced. As discussed previously in order to show effect of size, morphology and orientation of grains on the mechanical response is emphasized. Micron size tensile specimens and RVE FE analyses will be explained. With tensile specimens analyses, the attention is focused on thickness to grain size ratio (t/d) of specimens while with RVE calculations the analyses concentrate on morphological elongations and orientational alignments of different grain shapes.

3.1 Representative Volume Element (RVE)

In this thesis, for parametrization and grain morphology studies artificially generated representative volume elements (RVEs) are used. In this section, RVE generation and why it is used in analyses will be explained. Representative volume element (RVE) represents the smallest volume element that repeats itself throughout the total volume of the material at mesoscale and can imitate the general behavior and the mean properties of the material (see e.g. [54, 55]). RVE should be created such that it has large enough number of grains and it reflects all necessary morphological features of the material including grain shape and microdefects. It also should be small enough to be considered as a volume element in continuum mechanics.

These aforementioned artificial microstructures called RVEs are generated and meshed using Neper software through Voronoi tesselation (see [56]). An example of virtually created RVE microstructure is shown in Figure 3.1. For the Voronoi tesselation, dimensions of the space domain and either total grain number or mean grain diameter

have to be provided along with the desired statistical criteria such as mean aspect ratio and mean sphericity. Grains are nucleated from points called seeds. Seeds are distributed randomly to the domain and spherical growth is initiated from these seed points. Having computed the mean grain volume, growth is continued to fill the volume near each seed until the defined statistical criteria are satisfied. Voronoi tesselation method is employed extensively to create microstructure geometries and meshes in the literature. (see e.g. [57, 58, 59, 60, 55])

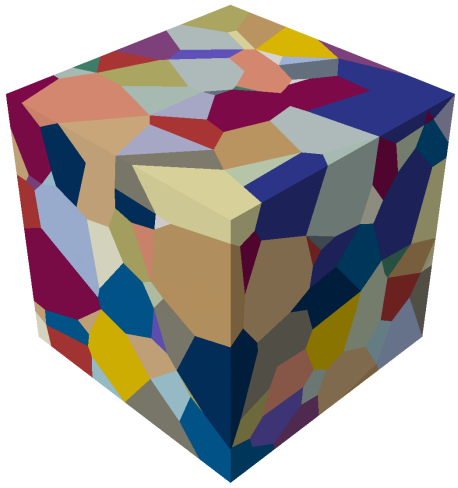

Figure 3.1: Virtually created RVE microstructure with 300 grains.

3.2 Implementation of Boundary Conditions

3.2.1 Boundary Conditions for Tensile Specimen Calculations

For tensile specimen analyses, boundary conditions are visualized in Figure 3.2. All the nodes of the bottom surface are constrained in Y direction while the node at the origin is constrained in all three directions. Moreover, x1 node is constrained in z-direction while z1 node is constrained in the x-direction to eliminate any possible rigid body rotation and ensure uniaxial tension.

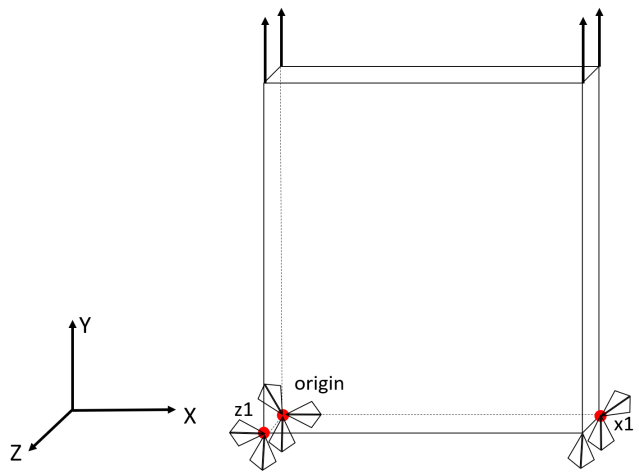

Figure 3.2: Boundary conditions for uniaxial tension simulation.

3.2.2 Boundary Conditions for Representative Volume Element Calculations

The boundary conditions for RVE calculations are adjusted such that RVE can imitate the mechanical response of the material. Also, to simulate the uniaxial tensile loading conditions stress triaxiality is enforced to remain constant at (T=1/3) throughout the entire loading. The stress triaxiality is defined as ratio of the hydrostatic stress to to the von Mises equivalent stress and can be written as,

$$T = \frac{\Sigma_h}{\Sigma_{eq}} \tag{3.1}$$

where Σ_h and Σ_{eq} are the hydrostatic stress and von Mises equivalent stress, respectively. Hydrostatic stress and equivalent von Misses stress are defined as,

$$\Sigma_h = \frac{\Sigma_{11} + \Sigma_{22} + \Sigma_{33}}{3} \tag{3.2}$$

$$\Sigma_{eq} = \frac{1}{2}\sqrt{(\Sigma_{11} - \Sigma_{22})^2 + (\Sigma_{11} - \Sigma_{33})^2 + (\Sigma_{33} - \Sigma_{22})^2} \tag{3.3}$$

With the imposed boundary conditions for the RVE analyses in this study, ratio of the hydrostatic stress to equivalent stress results in 1/3 after the homogenization procedure. Therefore, the triaxiality is enforced to remain constant at 1/3 and all the

surfaces of the RVEs are kept straight. To employ this boundary condition, first a master node M is selected on (L1, L2, L3) cube RVE. The coordinate for this node should be the (L1, L2, L3) as it is the corner of the RVE which enables us to couple the displacements of the surfaces and the master node. Surface names and master node on cube RVE with displacement directions are shown in Figure 3.3. Displacement couple equations for master node and the surface can be written as

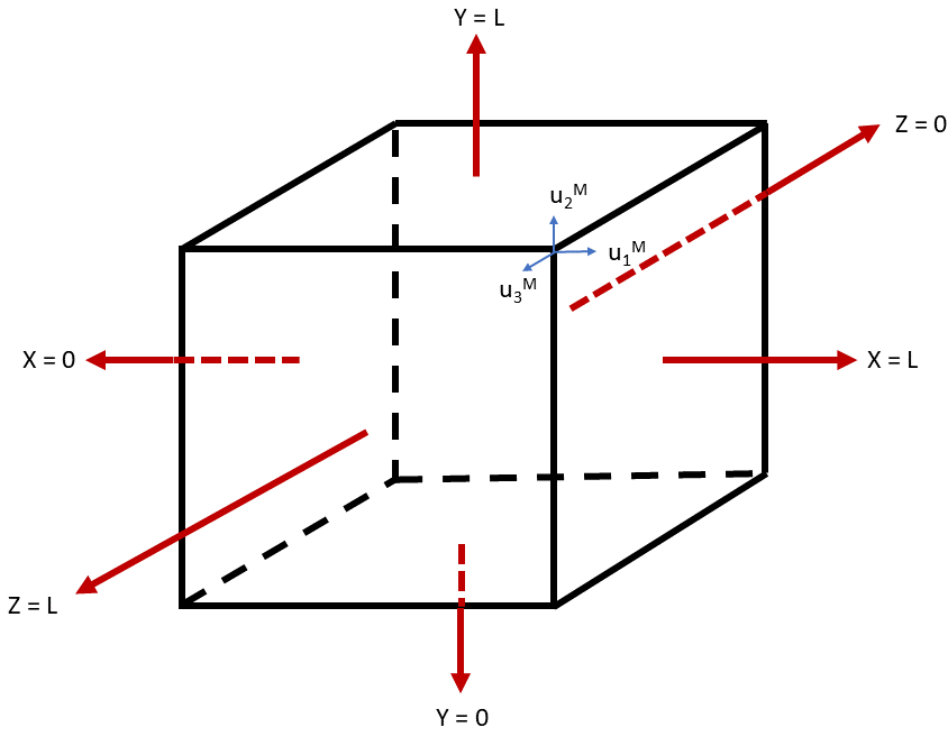

Figure 3.3: Location of master node and surfaces on RVE.

$$u_1(0, x_2, x_3) + u_1^M = 0 \tag{3.4}$$

$$u_1(L_1, x_2, x_3) - u_1^M = 0 \tag{3.5}$$

$$u_2(x_1, L_2, x_3) - u_2^M = 0 \tag{3.6}$$

$$u_3(x_1, x_2, 0) + u_3^M = 0 \tag{3.7}$$

$$u_3(x_1, x_2, L_3) - u_3^M = 0 \tag{3.8}$$

Bottom surface of the RVE is fixed in terms of u_2

$$u_2(x_1, 0, x_3) = 0 \tag{3.9}$$

With the above equations, every given displacement to node M is guaranteed to be fully supplied to relevant unit cell surfaces. More information about RVE boundary conditions covering other constant triaxiality values can be found in [61].

3.3 Homogenization

It is important to get a mesoscopic stress-strain response to analyze the results more accurately. Homogenization methods are particularly suited to capture the mechanical behavior of macroscopic scale from grain-scale calculations. The effective characteristics of heterogeneous materials can be obtained in this manner (see e.g [55], [60], [62], [63] for some examples in the literature).

This overall responses of RVEs can be obtained with the fundamental theorem of homogenization,

$$\Sigma_{ij} = \frac{1}{V} \int_V \sigma_{ij} \ dv \quad with(i, j = 1, 2, 3) \tag{3.10}$$

where Σ_{ij} is the mesoscopic stress components of the RVE, σ_{ij} is the microscopic Cauchy stress, and V is the total volume of the representative volume element. As a result, Σ_{ij} is determined for an RVE by summing the microscopic Cauchy stresses over each element with their associated integration points through

$$\Sigma_{ij} = \frac{\sum_{m=1}^{N} (\sum_{q=1}^{p} \sigma_{ij}^q v^q)^m}{V} \tag{3.11}$$

where N is the number of elements, p is the total number of integration points and v is the local volume at the integration point.

3.4 Parameter Identification

For the identification of material parameters an artificial representative volume element (RVE) is generated through Voronoi tessellation using Neper software with 300 grains. The material data for AA6016 in T4 temper condition in [64] is considered and the stress-strain response is fitted to the ones from the RVE computations. Symmetric boundary conditions with tensile loading which is explained in details in boundary conditions part are imposed such that all surfaces of RVE are kept straight and ensure that triaxiality values remain 0.33 (see e.g. [55]).

Cubic elastic parameters for aluminum sheet is taken as $C_{11} = 108.2$ GPa, $C_{12} = 61.3$ GPa and $C_{44} = 28.5$ GPa [65]. Reference slip rate $\dot{\gamma}_0$ is taken as 10^{-3} and rate sensitivity exponent n is determined as 60 for analyses to be rate-independent as much as possible. The ratio of latent hardening to self-hardening q is a constant for all grains and taken as 1.4 considering strong latent hardening for aluminum (see e.g. [51], [66]). After the identification process, the hardening parameters are obtained as, initial hardening modulus $h_0 = 190$ MPa, saturation slip resistance $g_s = 95$ MPa and initial slip resistance $g_0 = 47$ MPa. Additionaly, three different simulations with different sets of random orientations are conducted to verify the obtained hardening parameters, see Fig. 3.4. For both parametrization and main analyses, the strain rate is taken as 10^{-3}.

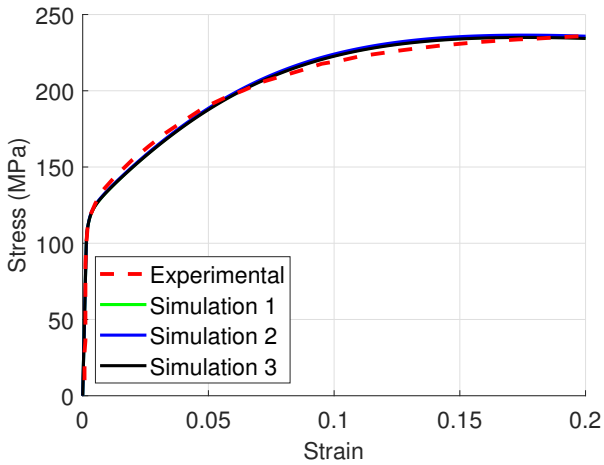

Figure 3.4: Comparison of stress strain responses of RVEs with fitted parameter and experimental study presented in [64]

3.5 Tensile Specimens

Tensile specimens are generated with 2 mm x 2 mm dimensions having varying thicknesses, see Table 3.1. Four example microstructures of the specimens are presented in Fig. 3.7. Grain orientations are assigned randomly for each grain where Euler ZYX convention is followed. The intervals for Euler angles are selected as $\phi[0\ 360]$, $\theta[0\ 180]$,$\psi[0\ 360]$.

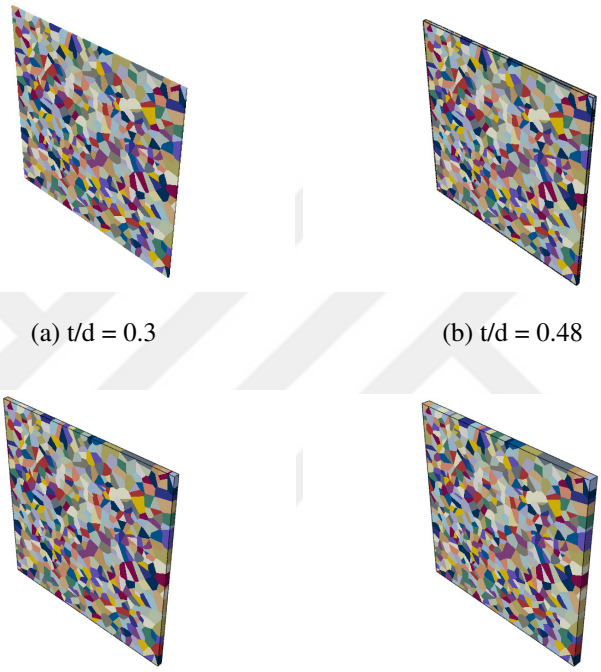

(a) t/d = 0.3 (b) t/d = 0.48

(c) t/d = 0.62 (d) t/d = 0.88

Figure 3.5: Microstructures of specimens having different t/d values below 1.

The employed local plasticity cannot predict the intrinsic size effect due to varying grain size. In order to include such effects a strain gradient crystal plasticity model should be used (see e.g. [67], [68], [69]). The variation of both grain size and the thickness makes the analysis complicated and it would be difficult to get a clear conclusion when both intrinsic and extrinsic size effect is active. Therefore as an initial attempt we keep the grain size around a constant value and vary the thickness using a size-independent model. In this way the hardening parameters are naturally kept constant in all simulations. The strategy of controlling the t/d ratio by changing

Table 3.1: Dimensions and corresponding t/d ratios of examined specimens.

thickness (μm)	mean grain diameter (μm)	t/d ratio	total number of grains
18	59	0.30	665
35	73	0.48	665
53	85	0.62	665
70	93	0.75	665
88	100	0.88	665
105	105	1	685
147	105	1.4	959
168	105	1.6	1096
189	105	1.8	1233
211	105	2	1370
232	105	2.2	1507
253	105	2.4	1644
274	105	2.6	1781
295	105	2.8	1918
316	105	3	2055
358	105	3.4	2329
400	105	3.8	2603
442	105	4.2	2877
484	105	4.6	3151
526	105	5	3425
568	105	5.4	3699

thickness is also conducted experimentally in literature (see e.g. [33], [70]). Note that the CPFE model does not include the effect of grain boundaries directly. For a more physical analysis where the influence of grain boundary orientation and the misorientation between the grains are considered, a proper GB model should be included in the modeling (see e.g. [68], [71]). In here the misorientation between the neighbouring grains create a constraining effect anyhow due to the different plastic-

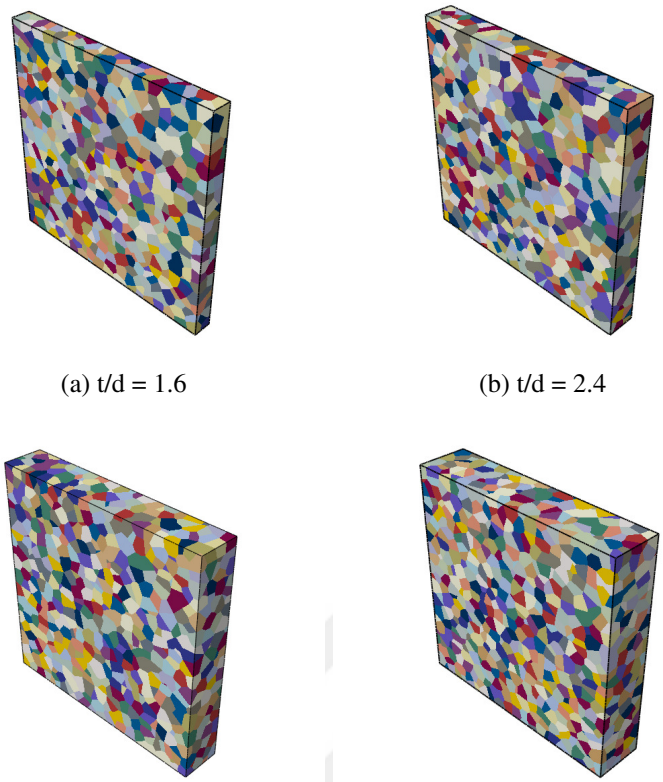

(a) t/d = 1.6 (b) t/d = 2.4

(c) t/d = 3.4 (d) t/d = 4.2

Figure 3.6: Microstructures of specimens having different t/d values above 1.

ity evolution coming from the random orientation distribution. Therefore, the model indirectly considers the effect of the grain boundaries with a limited capacity.

A mean grain size of 105 μm is considered for each specimen with t/d $>$ 1. The thickness of the specimens vary between 18 μm and 568 μm, which leads to t/d ratios within an interval between 0.3 and 5.4. To capture the critical value of the t/d ratio, the thickness is gradually increased until the increase in flow stress is almost levelled off. In order to preserve the mean grain size, the number of grains is increased from 685 (t/d=1.0) to 3699 (t/d=5.4) by increasing the thickness. On the other hand, the specimens having t/d ratio below 1 consist of 665 grains. Microstructures of these specimens can be seen in Figure 3.5.

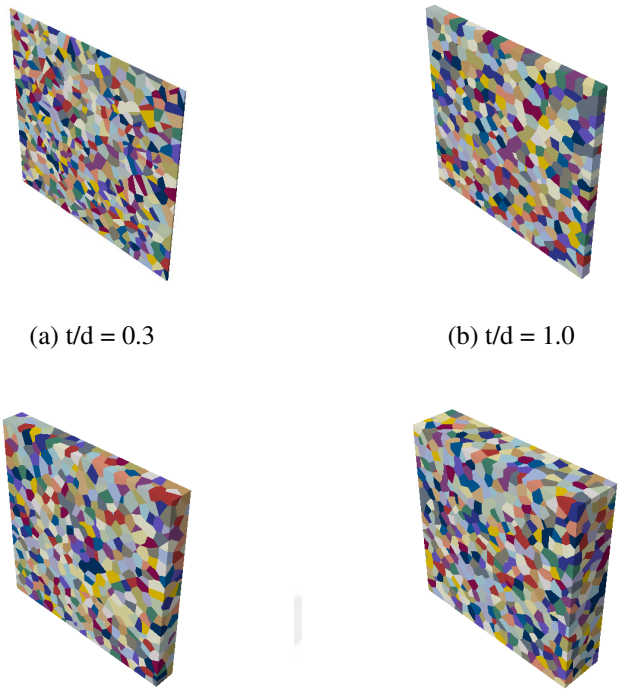

(a) t/d = 0.3 (b) t/d = 1.0

(c) t/d = 2.2 (d) t/d = 4.6

Figure 3.7: Microstructures of specimens having different t/d values.

3.6 RVE Analyses for Morphological and Orientation Study

To represent different morphologies, different representative volume elements (RVEs) are generated with 300 grains. The average aspect ratio of the grains is adjusted such that the first RVE has equiaxed grains, while other RVEs have grains in the shape of needles. Needle RVEs have the ratio of longer dimension to the shorter dimension from 2 to 10, separately. Equiaxed, needle1, needle2 and needle3 RVEs are shown in Fig. 3.8. These morphologies consist of grains with mean aspect ratios of (1,1,1), (0.5,1,0.5), (0.25,1,0.25) and (0.1,1,0.1), respectively where the ratio of longer dimension to the shorter dimension is gradually increased.

3.6.1 Crystal orientations for RVE Analyses

For the orientation of the grains, Euler ZYX convention is implemented. From the local coordinate system to the global coordinate system, crystals of each grain are

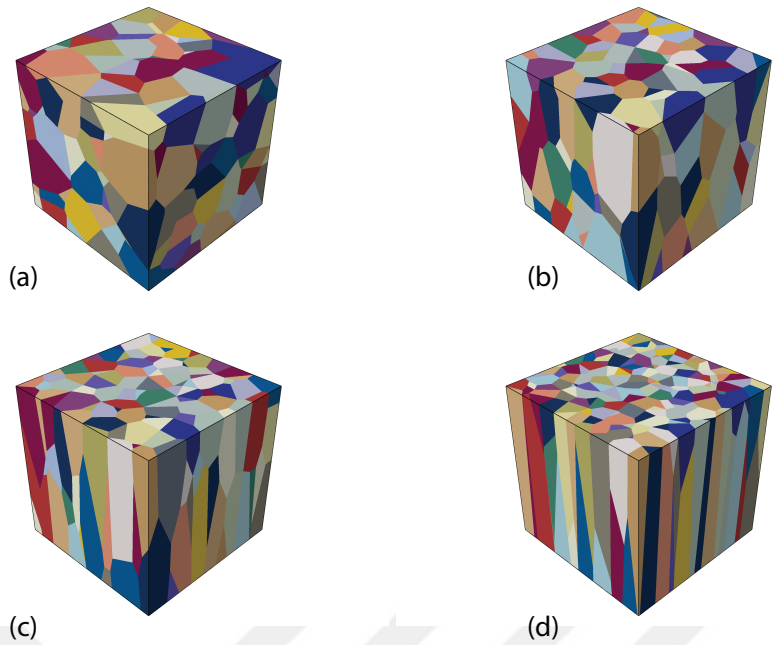

Figure 3.8: RVEs with different grain morphology; (a) Equiaxed, (b) Needle1, (c) Needle2, (d) Needle3

assigned to have a set of Euler rotations. In the case of the RVEs with randomly oriented grains, each grain has a unique set of Euler angles in the range of [0 360] for X and Z rotation and [0 180] for Y rotation. This set of angles provides the required randomness in terms of crystal orientation. Note that the local plasticity model used in the current study does not account for the effect of the grain boundaries through a specific model. Nevertheless, the crystal orientations are assigned randomly, so, there are orientation differences between adjacent grains which create such an effect that grains restrain each other from slip and rotation as if the model includes the grain boundaries.

For the RVEs with orientation alignment, grain orientations are distributed randomly within restricted intervals. Crystals are tilted around the building direction by imposing X and Z rotations while the Y rotation is always kept at zero. For instance, being oriented up to 10 degrees means an Euler transformation between local coordinates to global coordinates in such a way that the X and Z rotations are restricted to the interval of [-10 +10]. The rotation angles are selected randomly within their restricted intervals. The aim is to provide an orientation alignment to the material around the

building direction while preserving the polycrystalline characteristic.

3.6.2 Aligned Grain Orientations

To examine the orientation alignments clearly, a pole figure study is also conducted for RVE calculations with different crystal orientation restrictions. Pole figure is a way of graphical representation for analyzing the probability densities of grain orientation in a medium. How to read these figures is explained in section 2.4.

For an easier comparison between RVEs with different orientation restriction a relation of resultant angle to the building direction (BD) is used which is called mean resultant angle to BD. This mean resultant angle (MRA) relation can be calculated by rotation matrix using Euler angles. The input for the rotation matrix is taken by the average angle from the limits of the restriction and it is represented in Figure 3.9.

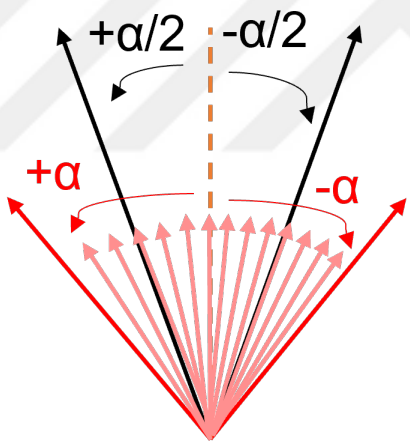

Figure 3.9: Corresponding $\alpha/2$ for the mean angle of rotation for rotation restriction between – α and + α

Calculation of MRA with rotation matrix is given by this relation

$$\begin{bmatrix} b_1 \\ b_2 \\ b_3 \end{bmatrix} = \begin{bmatrix} A_{11} & A_{12} & A_{13} \\ A_{21} & A_{22} & A_{23} \\ A_{31} & A_{32} & A_{33} \end{bmatrix} \begin{bmatrix} x \\ y \\ z \end{bmatrix} \tag{3.12}$$

where

$$A_{11} = cos(\theta)cos(\psi),$$
$$A_{12} = cos(\theta)sin(\psi),$$
$$A_{13} = -sin(\theta),$$
$$A_{21} = -cos(\phi)sin(\psi) + sin(\phi)sin(\theta)cos(\psi),$$
$$A_{22} = cos(\phi)cos(\psi) + sin(\phi)sin(\theta)sin(\psi),$$
$$A_{23} = sin(\phi)cos(\theta),$$
$$A_{31} = sin(\phi)sin(\psi) + cos(\phi)sin(\theta)cos(\psi),$$
$$A_{32} = -sin(\phi)cos(\psi) + cos(\phi)sin(\theta)sin(\psi),$$
$$A_{33} = cos(\phi)cos(\theta)$$

and calculation of mean resultant angle to BD (MRA) becomes

$$MRA = arccos\left(\frac{A_{11} + A_{22} + A_{33} - 1}{2}\right) \tag{3.13}$$

Examined pole figures of RVEs with different orientation restrictions are given in Table 3.2.

Table 3.2: Restricted intervals of RVEs with their corresponding mean resultant angles.

Z Rotation	Y Rotation	X Rotation	Mean Resultant Angle to the BD (MRA)
0	0	0	0
±1	0	±1	0.7
±5	0	±5	3.5
±10	0	±10	7.1
±15	0	±15	10.6
±20	0	±20	14.1
±25	0	±25	17.7
±30	0	±30	21.2
±35	0	±35	24.7
±40	0	±40	28.2
±45	0	±45	31.7
±50	0	±50	35.2
±55	0	±55	38.7
±60	0	±60	42.2
±65	0	±65	45.6
±70	0	±70	49.1
±75	0	±75	52.6
±80	0	±80	56.0
±85	0	±85	59.4
±90	0	±90	62.8
±95	0	±95	66.2
±100	0	±100	69.6
±105	0	±105	72.9
±110	0	±110	76.2
±115	0	±115	79.5
±120	0	±120	82.8
±125	0	±125	86.1
±130	0	±130	89.3

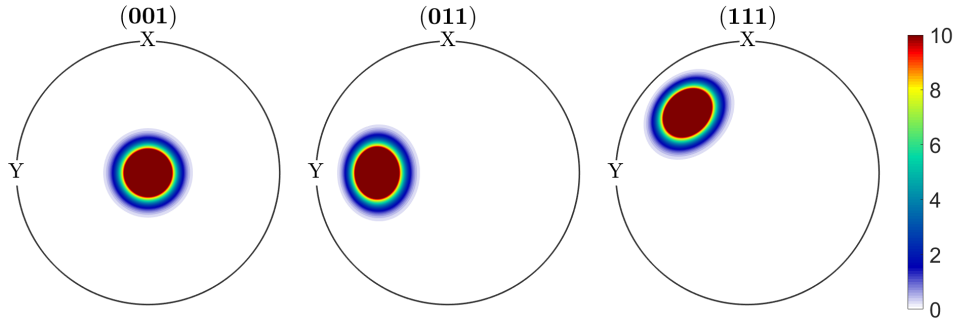

Figure 3.10: Pole figure for [-1 +1] & $0.7°$ MRA.

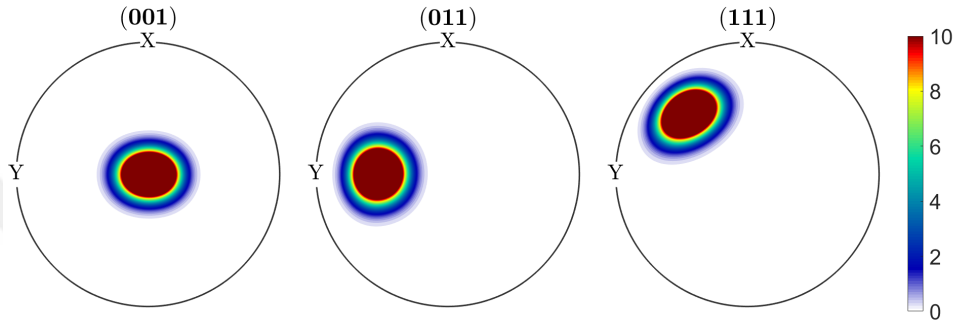

Figure 3.11: Pole figure for [-10 +10] & $7.1°$ MRA.

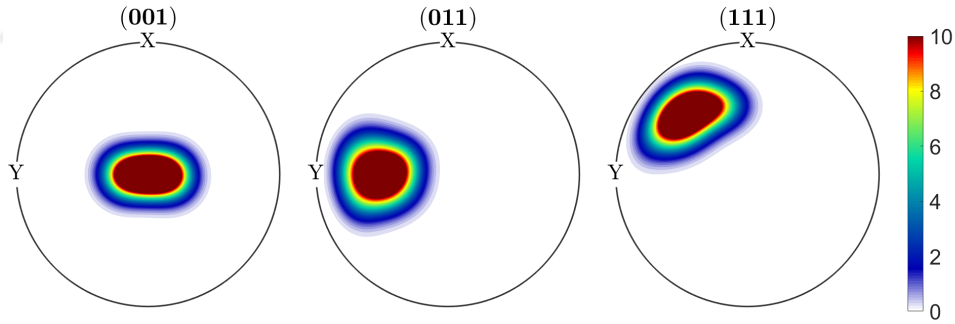

Figure 3.12: Pole figure for [-20 +20] & $14.1°$ MRA.

From Figure 3.10 to 3.20, distribution of crystal orientations are presented for different random orientation intervals. It can be concluded from these figures, for RVEs with more oriented along the building direction, less scatter is observed on the pole figures. Concentration of orientations can be seen with red areas on the figures. For RVEs with less oriented along the building direction, a more scattered drawing is obtained. As the orientation interval increases, pole figures oriented RVEs get close to RVE with fully random grain orientations.

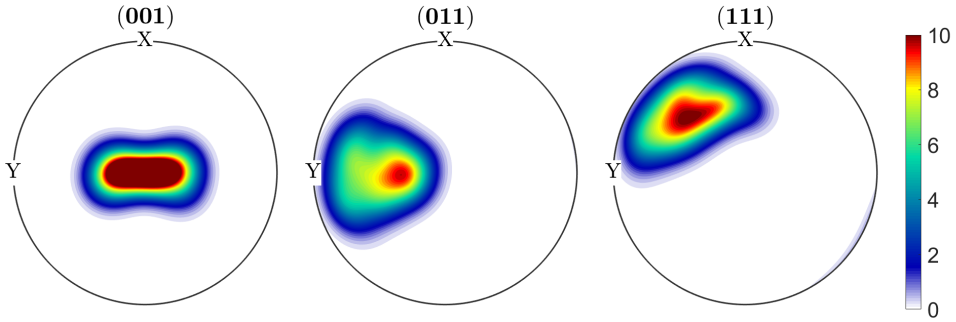

Figure 3.13: Pole figure for [-30 +30] & $21.2°$ MRA.

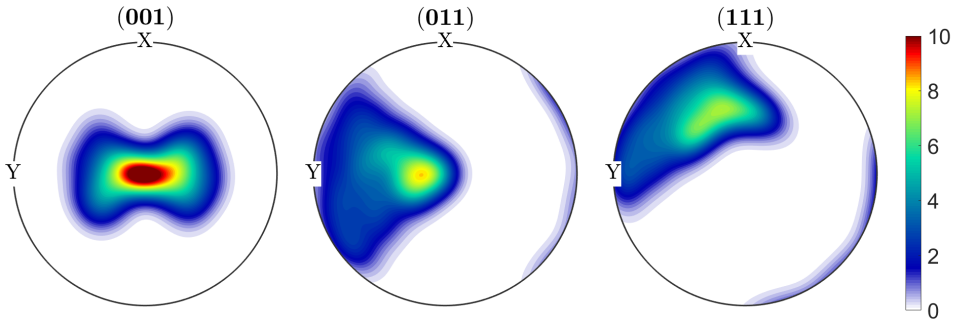

Figure 3.14: Pole figure for [-45 +45] & $31.7°$ MRA.

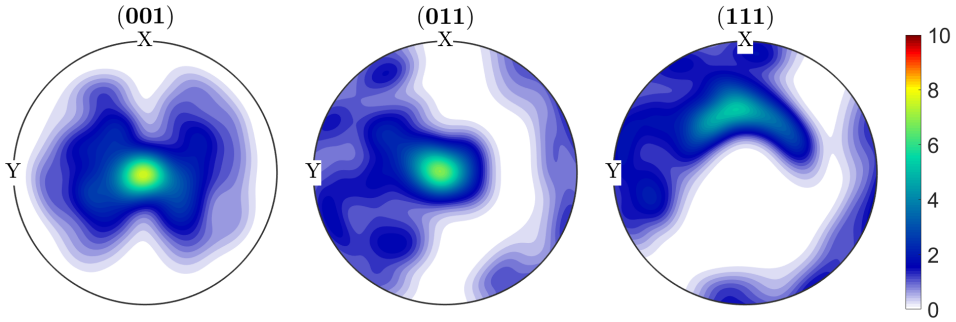

Figure 3.15: Pole figure for [-70 +70] & $49.1°$ MRA.

Another method for grain orientation alignment is applied. This time, grain orientations are arranged such that all the grains would have the same angle to the building direction rather than having a restricted interval. The difference between this method and the previously explained restricted interval is that when given a restricted interval, grain orientations are alternating within their prescribed interval whereas this method ensures all the grains have same mean resultant angle. For example, for the RVE with grains having $10°$ to the building direction, all the grains are still oriented randomly,

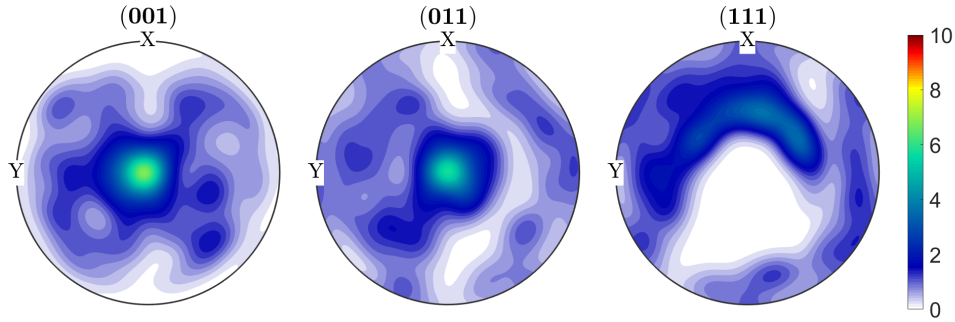

Figure 3.16: Pole figure for [-80 +80] & $56°$ MRA.

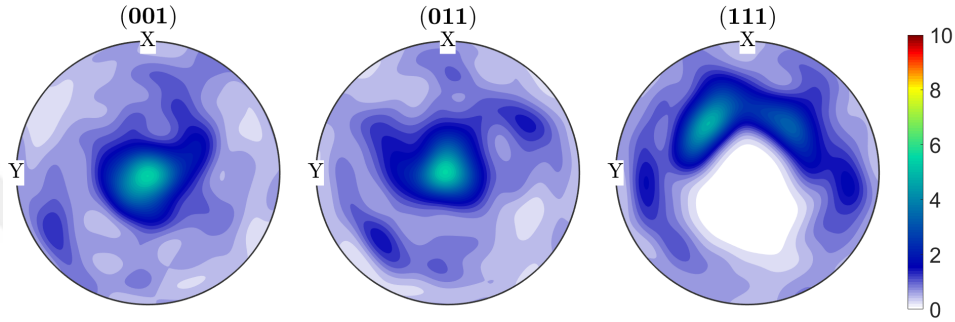

Figure 3.17: Pole figure for [-90 +90] & $62.8°$ MRA.

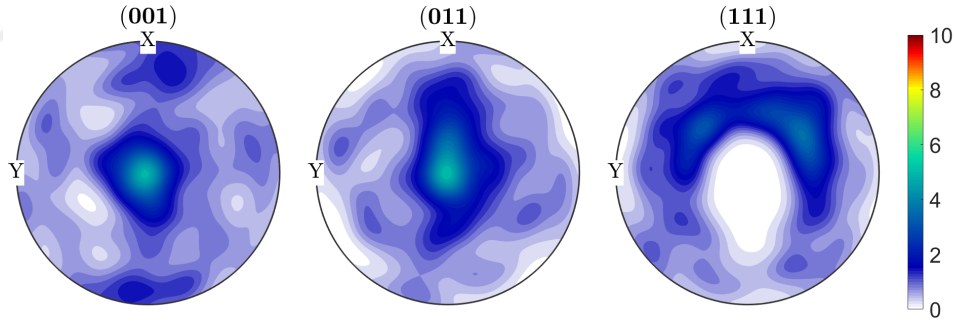

Figure 3.18: Pole figure for [-110 +110] & $76.2°$ MRA.

in other words, they have different amount of X and Z rotation but it is settled that they all have the 10 degrees as the resultant angle. Analysed RVEs with grains having corresponding angles are presented in Table 3.3. Pole figures of these RVEs are shown from Figure 3.21 to 3.29.

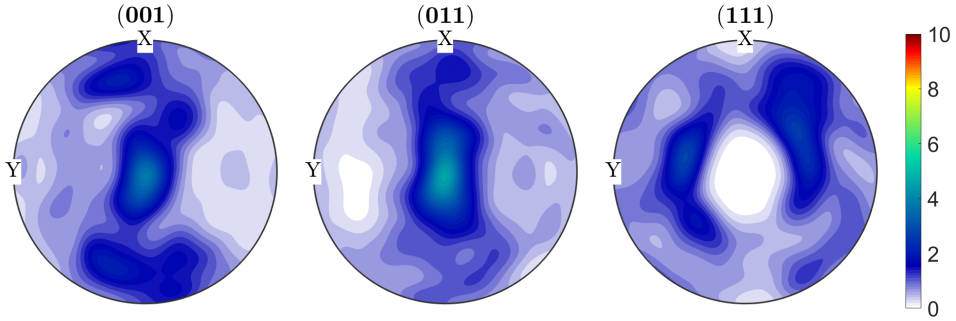

Figure 3.19: Pole figure for [-130 +130] & $89.3°$ MRA.

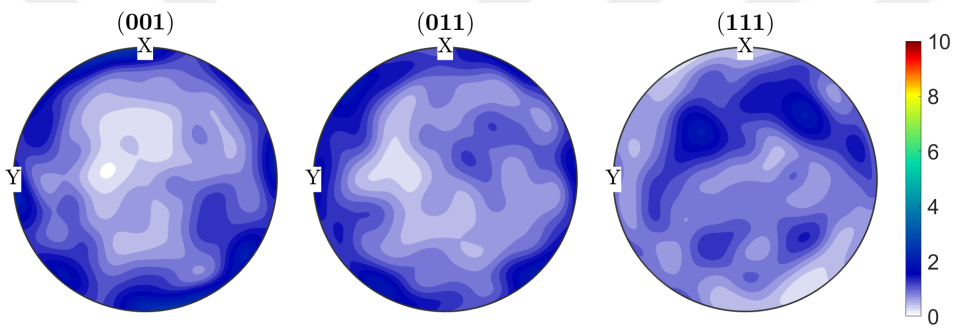

Figure 3.20: Pole figure for full randomly oriented RVE.

Table 3.3: Resultant angles of grains for different RVEs when all the grains having same angle to BD is maintained .

RVE number	Resultant Angle	RVE number	Resultant Angle
1	5	7	50
2	10	8	60
3	20	9	70
4	30	10	75
5	35	11	80
6	40	12	90

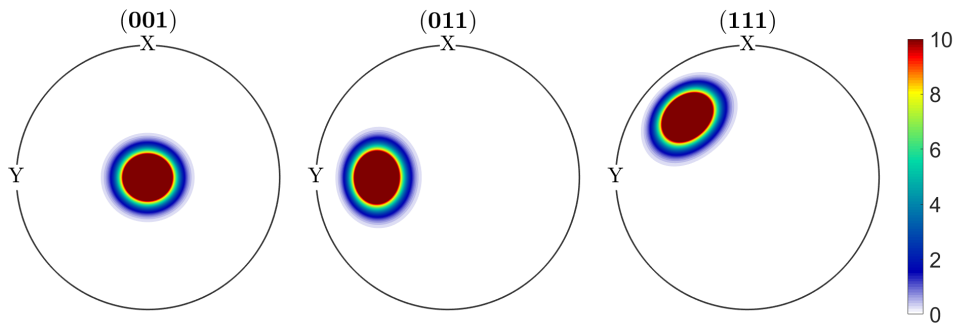

Figure 3.21: Pole figure for RVEs with all grains having 5° resultant angle.

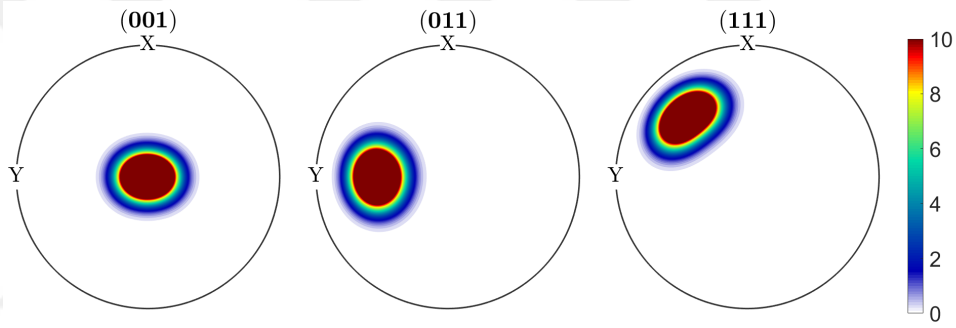

Figure 3.22: Pole figure for RVEs with all grains having 10° resultant angle.

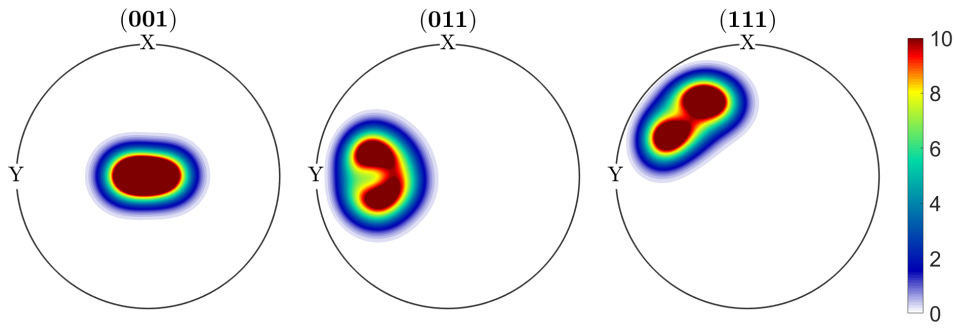

Figure 3.23: Pole figure for RVEs with all grains having 20° resultant angle.

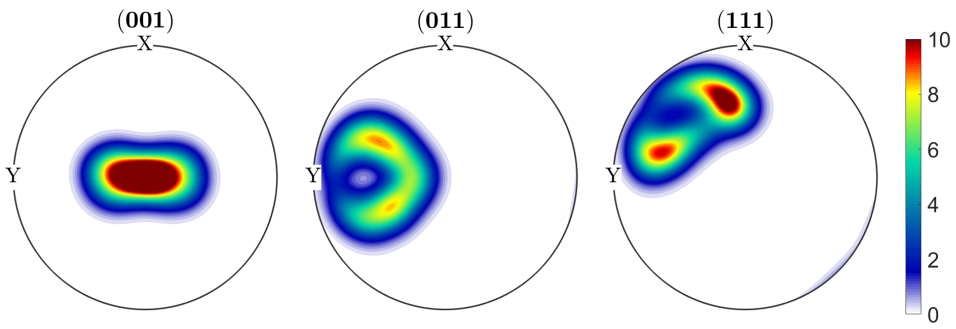

Figure 3.24: Pole figure for RVEs with all grains having 30° resultant angle.

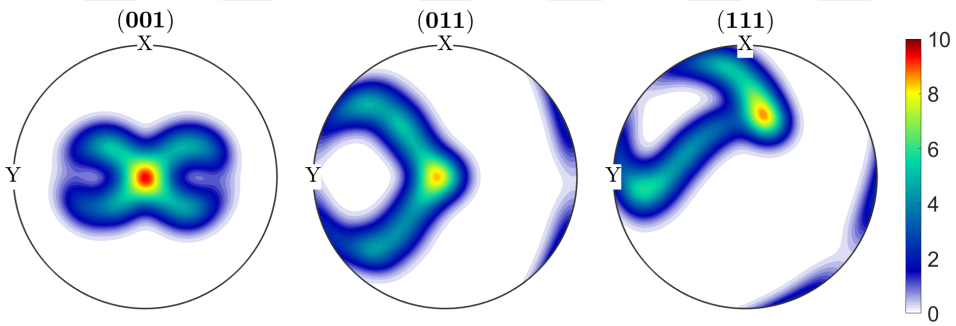

Figure 3.25: Pole figure for RVEs with all grains having 50° resultant angle.

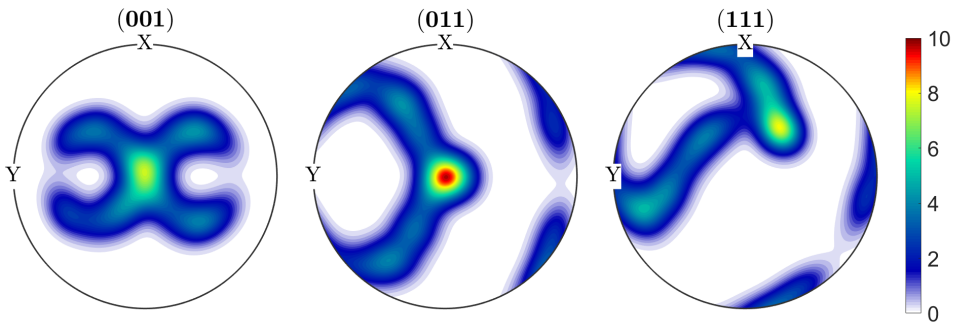

Figure 3.26: Pole figure for RVEs with all grains having 60° resultant angle.

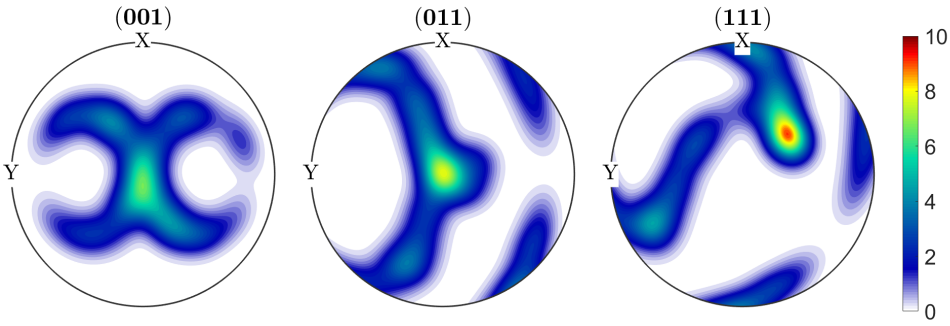

Figure 3.27: Pole figure for RVEs with all grains having 70° resultant angle.

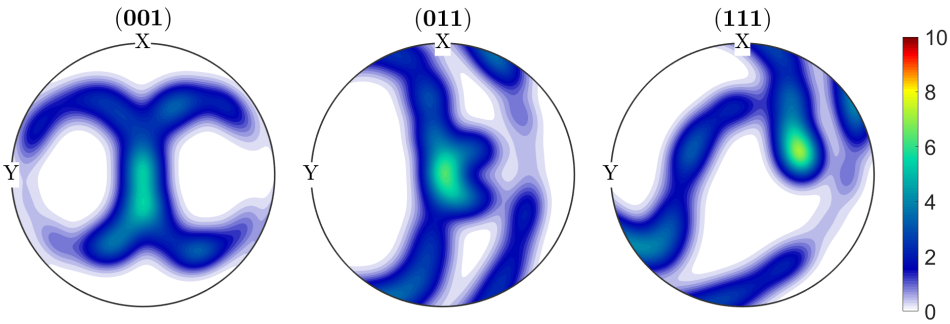

Figure 3.28: Pole figure for RVEs with all grains having 80° resultant angle.

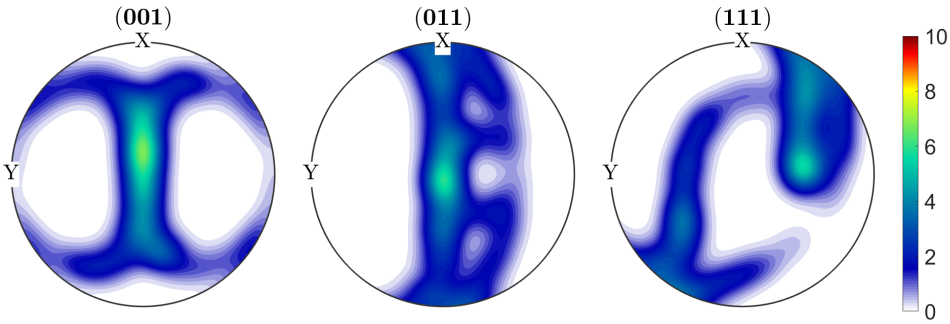

Figure 3.29: Pole figure for RVEs with all grains having 90° resultant angle.

CHAPTER 4

RESULTS AND DISCUSSIONS

Using the finite element models for micron size specimens and the representative volume elements described in the previous chapter, numerical examples are provided and the findings are discussed in this chapter. The results from the RVE analyses are first shown in the context of morphology and orientation, and then micro specimen results are shown in the context of thickness to grain size ratio effect.

4.1 RVE Analyses

Initially, the influence of the grain shape is addressed without considering the texture effect. In order to analyze solely the effect of the grain morphology, the orientations in all RVEs with different aspect ratios are assigned randomly. The CPFE simulations are conducted by imposing 10% displacement both in the building direction and the normal direction separately.

For both building and normal direction loading, the difference between constitutive response of RVEs is found to be negligible, as shown in Fig. 4.1. Although the grains are elongated gradually and reach a very columnar grain structure in needle3 case, the stress curves of the needle RVEs are very similar to that of equiaxed RVE. Even though the morphology has changed a lot, the crystal orientation of each grain is kept fully random in all RVEs in this simulation set. Considering the local plasticity model employed, the morphology itself did not make a significant difference. Morphologic differences without corresponding crystal orientation alignment are proven to be not much influential in the current numerical analysis. The possible usage of a strain gradient crystal plasticity model (see e.g. [67], [68], [69]) would be quite problematic

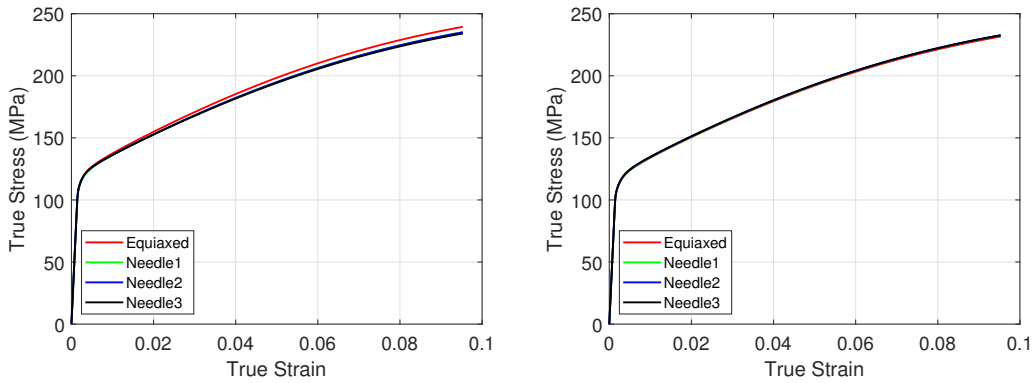

(a) Building direction loading

(b) Normal direction loading

Figure 4.1: Stress versus strain response for different microstructures with random orientations loaded in building and normal directions.

in this case due to the change in the mean grain size. Such a change would give non-physical results with considerable hardening.

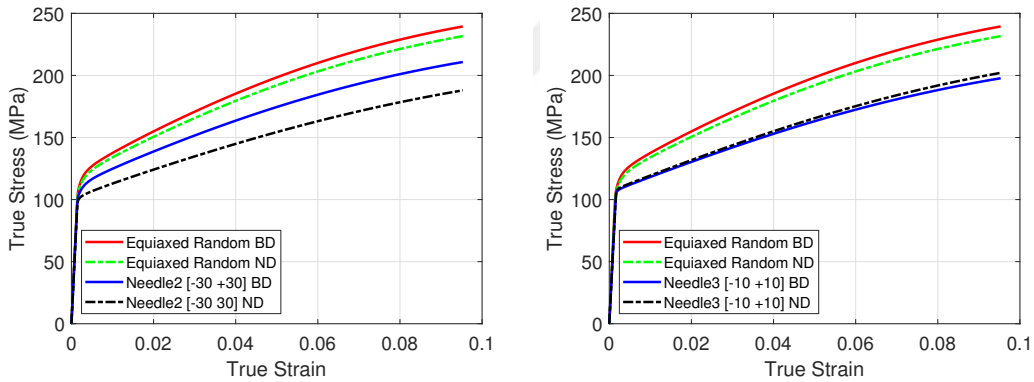

(a) Comparison of equiaxed and needle2

(b) Comparison of equiaxed and needle3

Figure 4.2: Stress versus strain response for different microstructures loaded in building (BD) and normal direction (ND).

To have more realistic microstructures, the crystal orientations are assumed to be evolved with the elongation of the grains, i.e. aligned in the building direction. For the reference state unrestricted, fully random, orientations are assigned to the RVE with equiaxed grains. Then, the orientations are gradually restricted in narrower intervals as grains are more elongated along the building direction. Both X and Z rotations

are restricted in [-90 +90], [-30 +30] and [-10 +10] intervals for RVEs called needle1 needle2 and needle3, respectively.

Fig. 4.2 demonstrates the stress versus strain response of RVEs having equiaxed and needle grains with corresponding orientation alignments. The first observation is that RVEs with elongated and textured grains possess weaker stress response compared to the RVE with randomly oriented equiaxed grains. For the textured RVEs, when the interval of orientation is kept in a narrower range, the orientations of individual grains become closer to each other. Since grains are oriented similarly, the indirectly imposed effect of the grain boundaries (misorientation) becomes more difficult to observe, especially for needle3. Since the the influence of the grain boundaries is still valid for the RVEs with the randomly oriented grains, they show higher resistance to the plastic deformation. Also, as illustrated in Fig. 4.2a, needle2 shows different responses for loadings in building and normal directions. Having grain orientations restricted in [-30 +30] interval, needle2 presents an anisotropic behaviour. On the other hand, randomly oriented RVE shows similar responses in both directions due to its isotropic structure. Likewise, as shown in Fig. 4.2b, strongly oriented needle3 also possesses similar responses for building and normal directions, but the reason for that is the crystal symmetry since the rotation angles are very small.

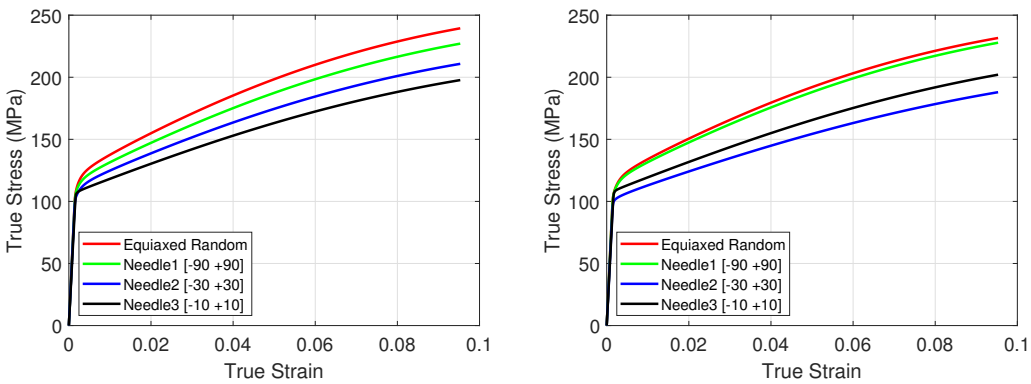

(a) Building direction loading

(b) Normal direction loading

Figure 4.3: Stress versus strain response for microstructures with different morphologies and orientation alignment.

Stress-strain response curves of all RVEs are illustrated in Fig. 4.3 for loading along

the building and the normal directions, separately. For both cases, the strongest response is obtained for the RVE with randomly oriented equiaxed grains. As the grains are more elongated and crystal orientations are further restricted, the stress response is decreased. For the normal direction loading, the stress response of needle2 is lower than the response of needle3, due to the plastic anisotropy observed in needle2, as discussed earlier.

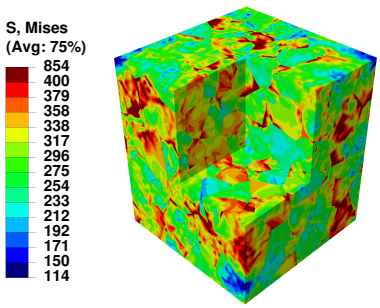

(a) Von Mises stress distribution of equiaxed RVE

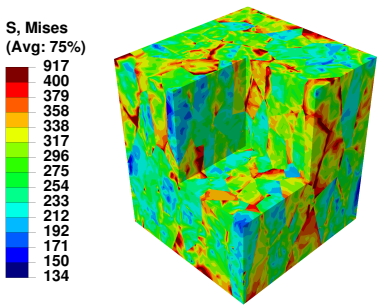

(b) Von Mises stress distribution of needle1 RVE

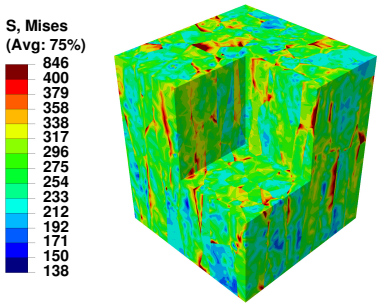

(c) Von Mises stress distribution of needle2 RVE

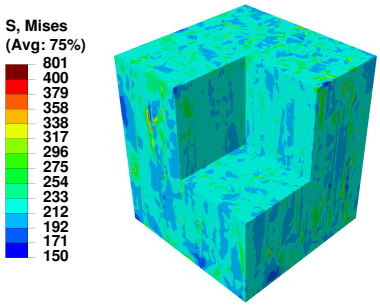

(d) Von Mises stress distribution of needle3 RVE

Figure 4.4: Von Mises stress distribution for different microstructures loaded in the building direction.

Von Mises equivalent stress contours for building and normal direction loadings are shown in Figs. 4.4 and 4.5 respectively. The lower stress response for RVEs with elongated and oriented grains can also be observed in von Mises stress distributions. Moreover, as the orientation alignment is increased, due to the diminishing of the misorientations between neighboring grains, more homogeneous stress distribution is observed in Figs. 4.4d and 4.5d.

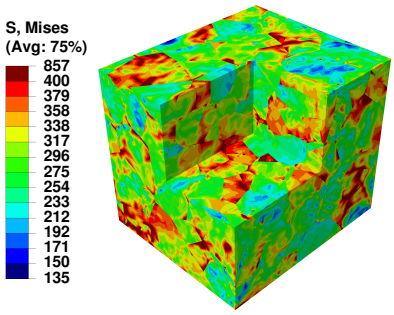

(a) Von Mises stress distribution of equiaxed RVE

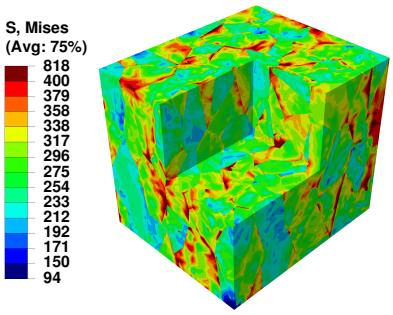

(b) Von Mises stress distribution of needle1 RVE

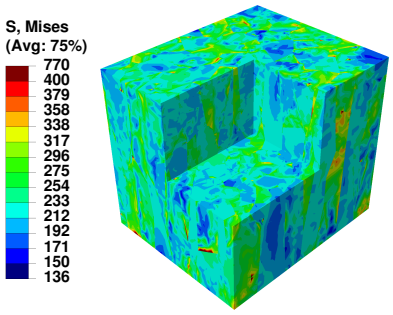

(c) Von Mises stress distribution of needle2 RVE

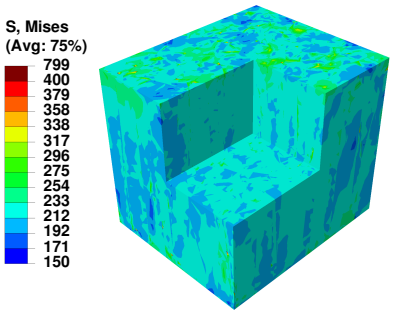

(d) Von Mises stress distribution of needle3 RVE

Figure 4.5: Von Mises stress distribution for different microstructures loaded in the normal direction.

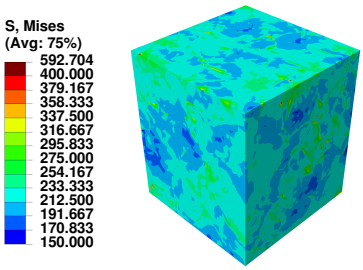

(a) Von Mises stress distribution of RVE with [-10 +10] & 7.1° MRA orientation restriction

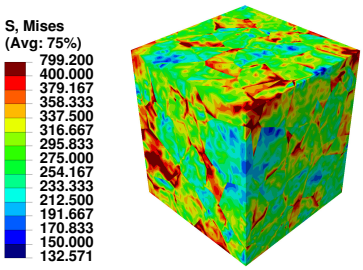

(b) Von Mises stress distribution of RVE with [-40 +40] & 28.2° MRA orientation restriction

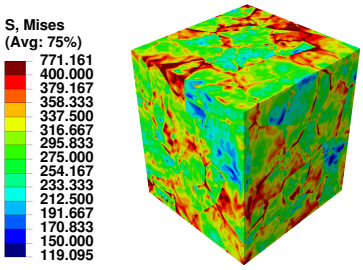

(c) Von Mises stress distribution of RVE with [-65 +65] & 45.6° MRA orientation restriction

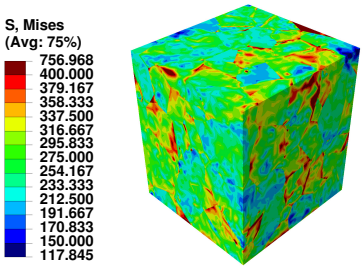

(d) Von Mises stress distribution of RVE with [-125 +125] & 86.1° MRA orientation restriction

Figure 4.6: Von Mises stress distribution for equiaxed morphology RVEs with different orientation restrictions.

After concluding that, the effect of morphology does not have a significant impact without the orientation alignment, a more comprehensive study is conducted about the orientation alignments with equiaxed RVEs. The stress results for 0.1 strain are given in Figure 4.7. Change in stress results shows similar trend with the experimental studies in literature. It can be seen from the figure that, stress result reaches maximum nearly 45 degree MRA about the building direction. Blue line on the figure indicates the result of RVE with full randomly oriented grains.

The study by giving random orientation to grains while maintaining that they will have same amount of resultant angle to building direction is conducted. True stress results are plotted in Figure 4.8. Similiar trend in Figure 4.7 can be observed. However, with this method a greater stress variation is observed.

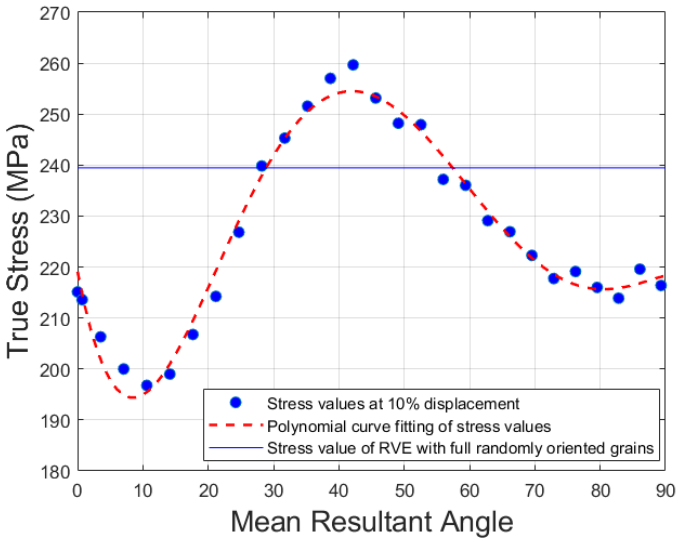

Figure 4.7: Stress vs Mean Resultant Angle for RVEs with restricted grain orientations at 10% displacement.

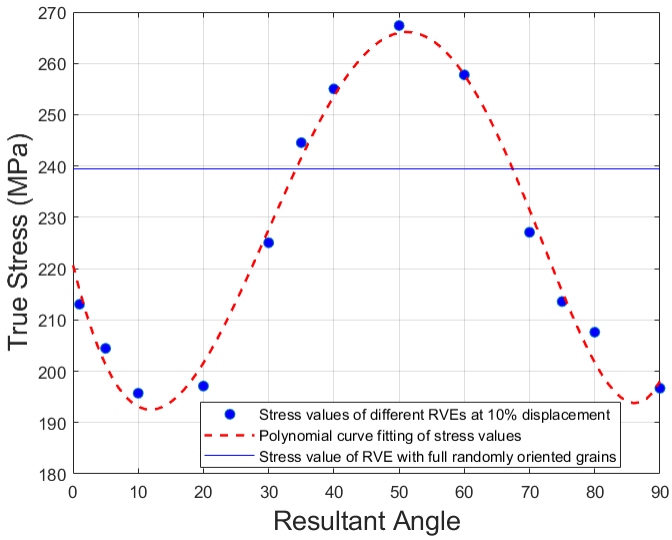

Figure 4.8: Stress vs Resultant Angle for RVEs with grains having exact resultant angle at 10% displacement.

4.2 Tensile Specimen Results for t/d Effect

In the simulations, a general trend of increase in flow stress with increasing t/d ratio is observed, which is obtained solely through thickness increase. In this analysis the

number of grains should be increased to see the influence of higher t/d ratios. Even though the total grain number is increased, the number of grains at the free surfaces stays nearly constant for all t/d ratios. Therefore, the ratio of the surface grains to all grains decreases for increasing t/d. As discussed previously, higher the surface grain ratio weaker the stress response. The results presented in Fig. 4.9 confirm this simple relation where the flow stress increases with increasing t/d and with decreasing surface grain ratio. At t/d equals 1, almost all grains are surface grains and the stress response is lowest among the other specimens having higher t/d. In Fig. 4.9a, it can be observed that flow stress increases rapidly with increasing t/d but then the rate of increase slows down. Fig. 4.9b shows that the increasing trend in flow stress diminishes for higher t/d ratios and the results converge to a single curve, which is expected for a polycrystalline material.

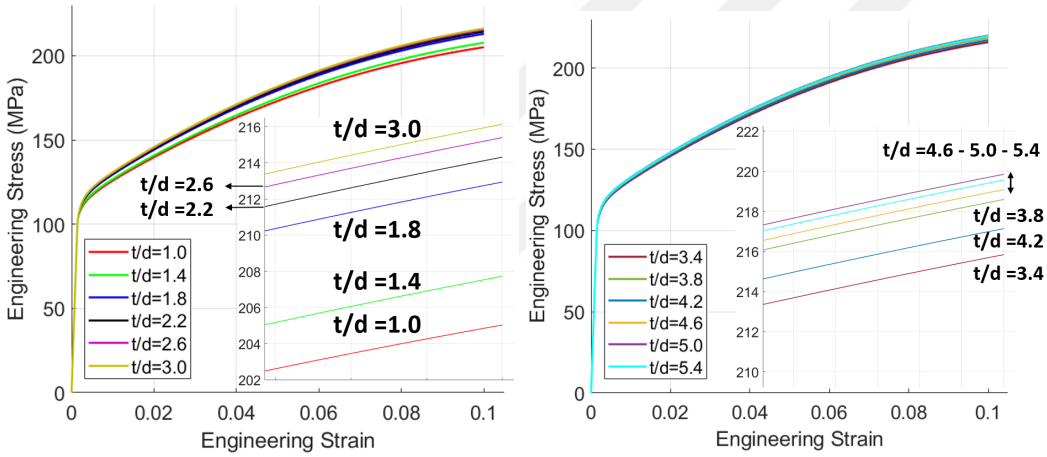

(a) Engineering stress-engineering strain curves of specimens having t/d below 3

(b) Engineering stress-engineering strain curves of specimens having t/d above 3

Figure 4.9: Engineering stress-engineering strain curves for specimens having different t/d ratios at 10% displacement.

To get a better comparison with the experimental behavior shown in Fig. 1.4, the flow stress values at different macroscopic strains are plotted for specimens having different t/d values in Fig. 4.10. In the experimental studies, flow stresses do not change much for specimens with t/d $<$ 1. When the ratio is increased further until the critical value, flow stresses are observed to be increasing rapidly. Above the critical value, the increase slows down and similar flow stress values are recorded for higher t/d ra-

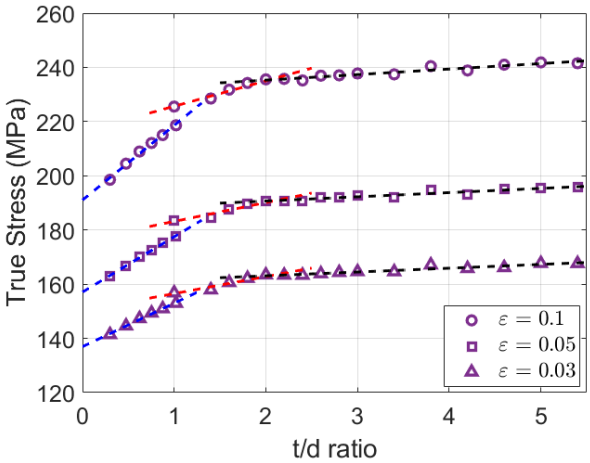

Figure 4.10: Flow stress values at different strains of specimens having different t/d ratios.

tios. In the current numerical study, the most obvious difference with experiments is obtained for t/d < 1 where a considerable increase in flow stresses occur. One of the reasons is that, in our simulations, the imposed boundary conditions make the specimen deform homogeneously, therefore it delays the localization. Another reason is that, even though the surface grain ratios are similar, the amount of grain boundaries changes dramatically for these specimens. Moreover, the most important reason is that in the calculations the same hardening parameters are used for each specimen. Yet, while specimens with t/d > 1 have the same mean grain size, the specimens with t/d < 1 show decreasing grain size behavior with decreasing t/d ratio. If hardening parameters were adjusted according to the grain sizes, or if a size dependent crystal plasticity model was employed, which would lead to a harder response, then the results would be similar for t/d < 1 to the experimental observations.

The flow stress response shows a steep increase for t/d between 1 and a critical value compared to the response at higher t/d ratios which converge to polycrystalline behavior. Fig. 4.10 shows that the critical value corresponds to around 2. Between 1 and the critical value, the numerical study resulted in a similar trend with the experimental results. Starting from t/d = 1, as the ratio is increased, the grain boundaries parallel to the loading direction start to emerge. These GBs contribute to the resistance of the material to plastic deformation. The difference between flow stresses is

not high compared to the experimental studies. The main reason is that the local crystal plasticity method does not include the effect of the grain boundaries directly as it was explained in the simulations section. Yet, there is a distinguishable evolution that constitutes observable trends. The influence of the boundary conditions which leads to same homogeneous behavior in all specimens could influence the difference between the experiments and the numerical results. While in experimental studies the thinner specimens start to localize earlier, here there is no difference in that regard due to homogeneous behavior. As stated previously, the increase in flow stress diminishes after the critical value. The findings of the simulations are parallel to the experiments. For these specimens, at least 2 grains are present through thickness and all grains have at least one horizontal grain boundary. Therefore, newly formed grain boundaries do not create a significant difference in flow stress. As the t/d ratio further exceeds the critical value, the mechanical response approaches to that of the bulk specimen and the effect of having few grains per thickness disappears.

The von Mises stress distributions of some specimens with t/d ratios below 1 is shown in Figure 4.11 and some specimens with t/d ratios above 1 is shown in Figure 4.12. To get a better outlook, the von Mises stress distributions of specimens with different t/d ratios from different t/d intervals are shown in Fig. 4.13. The difference in stress distribution is apparent especially on the lateral (thickness) surface. As the t/d ratio increases, a general increase in the von Mises stress values is apparent. The emergence of new GBs can be observed by examining the stress variation along the upper and lateral surfaces.

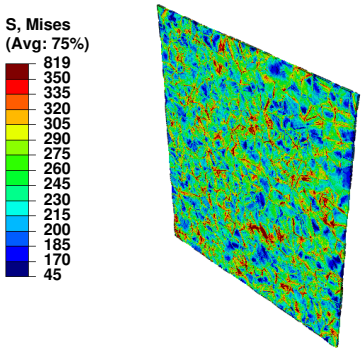

(a) t/d = 0.3

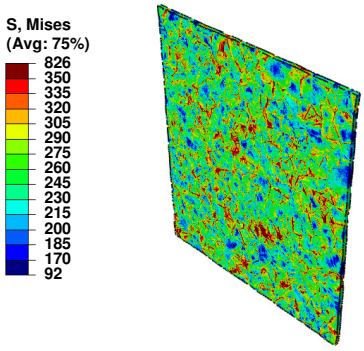

(b) t/d = 0.48

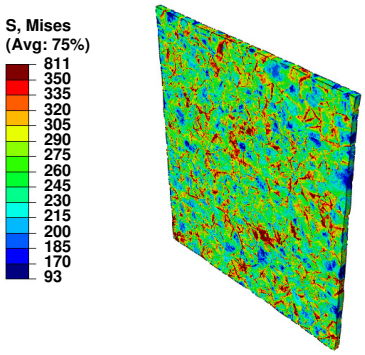

(c) t/d = 0.62

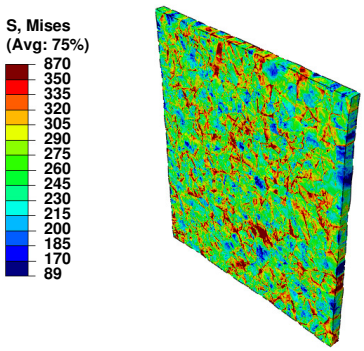

(d) t/d = 0.88

Figure 4.11: Von Mises stress distribution of specimens having different t/d ratios below 1 at 10% displacement.

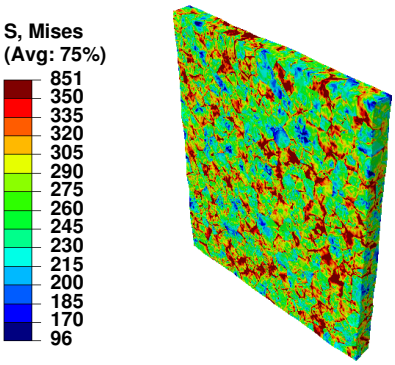

(a) t/d = 1.6

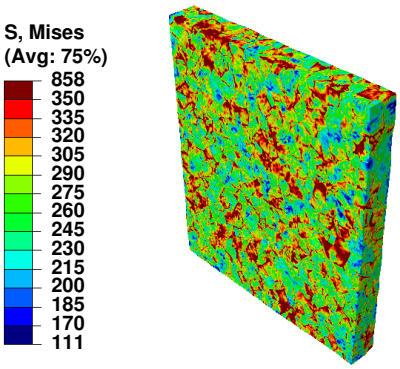

(b) t/d = 2.4

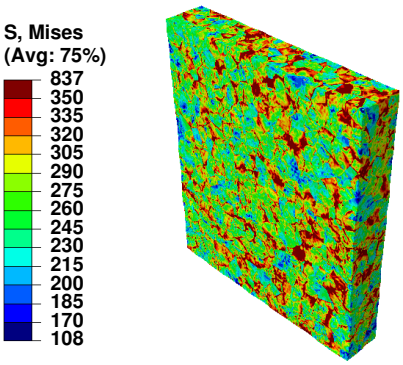

(c) t/d = 3.4

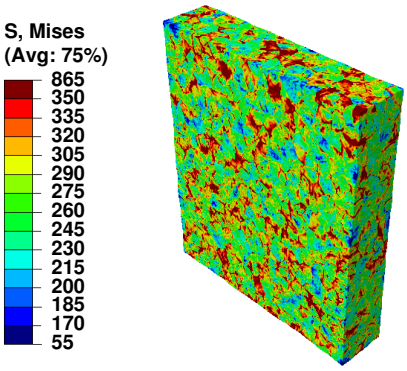

(d) t/d = 4.2

Figure 4.12: Von Mises stress distribution of specimens having different t/d ratios above 1 at 10% displacement.

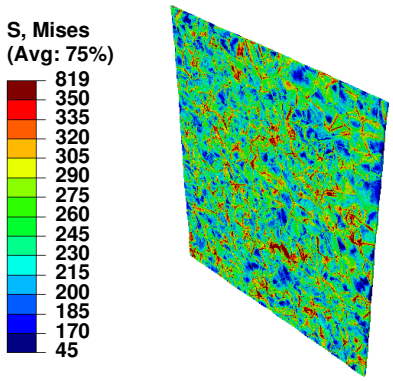

(a) t/d = 0.3

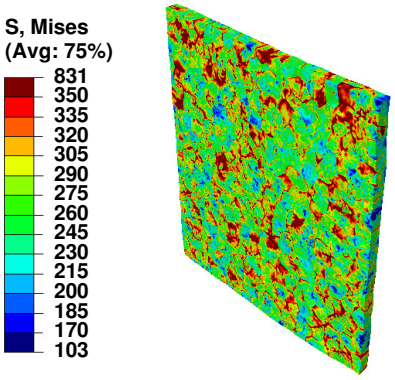

(b) t/d = 1.0

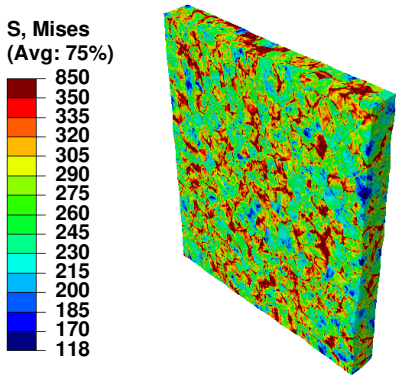

(c) t/d = 2.2

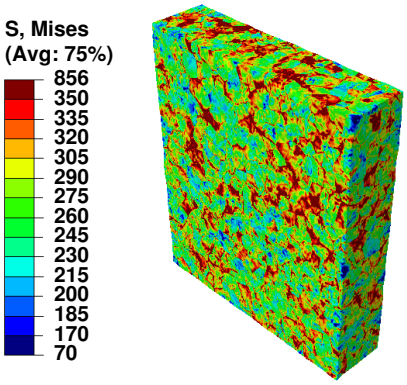

(d) t/d = 4.6

Figure 4.13: Von Mises stress distribution of specimens having different t/d ratios at 10% displacement.

CHAPTER 5

CONCLUSIONS

In this work, the crystal plasticity finite element method is initially employed to assess the effect of anisotropic grain structure with orientation alignments on the macroscopic behavior of additively manufactured metallic materials following a multi-scale approach. Then the influence of the of thickness to grain size ratio on micron size tensile specimens is addressed. The conclusions obtained from the RVE analysis and the full size micron tensile specimens are presented separately below with outlooks.

5.1 RVE Analyses for Anisotropic Grain Structure

With RVE analyses the mechanical behavior of the microstructures with columnar grains which are observed in additively manufactured metallic products is investigated through a crystal plasticity framework. Firstly, the sole effect of morphology is studied by modeling the RVEs with different degree of columnar structure having randomly oriented grains, however the difference between the constitutive responses is found to be negligible. After that, columnar grain structure and the corresponding orientation alignment are numerically modeled to assess the constitutive response and the anisotropy due to additive manufacturing. Step by step, the grains are elongated and the orientations are restricted around the building direction to analyze the anisotropy at different levels. After assigning the corresponding restricted orientations to the morphologies, a significant difference occurs between flow stresses of RVEs with equiaxed and columnar grains for both building and normal direction loading. The stress response weakens as grains become more columnar. RVEs with grains oriented around the building direction demonstrates that when the orientation of each

grain is assigned in a similar direction, the misorientation of the neighboring grains diminishes.

A more comprehensive study about the grain orientation restriction showed that there is significant change in stress responses with varying mean resultant angle. As the mean orientation angles come close to 45 degree, resistance to plastic deformation gets stronger. Mean orientations beyond the 45 degree, flow stresses starts to result in lower values. Since the misorientations indirectly impose the effect of the grain boundaries, oriented RVEs show different mechanical responses. The numerical results agree qualitatively with the literature (see e.g. [28], [72]). Final crystalline structure of additively manufactured products have significant importance in terms of mechanical properties.

Note that the current study considers solely the influence of the grain morphology and the induced lattice allignment on the macroscopic anisotropic response through a local crystal plasticity model which cannot predict the size effect. However the evolution of such elongated grain structure raises the question of the mean size of the grains and related size effect which should be addressed through a nonlocal crystal plasticity framework. Moreover the current work does not include the influence of the porosity evolving during the additive manufactiuring processes. In order to understand the effect of the microstructure the cavities should be incorporated as well.

5.2 t/d Effect on Full Size Micron Specimens

The macroscopic response of the specimens are compared with the experimental findings in the literature in a qualitative manner. For specimens with thickness to grain size ratio t/d < 1, the numerical results were not in an agreement with the experiments. Significant differences between flow stresses of the specimens were observed even though similar values were recorded in experimental studies. The most important reason was the same hardening parameters being used for specimens with different mean grain sizes, which would naturally decrease in the t/d < 1 regime. A more accurate study can be conducted in the future with appropriate hardening parameters or by employing a strain gradient crystal plasticity model which would take into account

the intrinsic size effect would naturally decrease in the t/d < 1 regime.

For t/d > 1, flow stresses increase rapidly until the critical value. The critical value is found to be approximately 2. The rapid increase was a result of the development of the GBs parallel to the loading direction. The trend is in line with the empirical tests in literature, yet the differences between flow stresses were lower in simulations compared to the experiments due to the employed local crystal plasticity model which cannot include the direct effect of the GBs. Further increase in the t/d ratio, above the critical value, slows down the increase in flow stress. Since there is already a considerable amount of GBs parallel to the loading direction, newly formed GBs do not make a substantial contribution to the resistance to deformation. Moreover, for specimens with higher t/d ratios, the specimens can no longer be treated as thin specimens and the behavior converges to the polycrystalline one.

REFERENCES

[1] B. J. A. Dorussen, M. G. D. Geers, and J. J. C. Remmers, "A discrete element framework for the numerical analysis of particle bed-based additive manufacturing processes," *Engineering with Computers*, 2022.

[2] M. M. Francois, A. Sun, W. E. King, N. J. Henson, D. Tourret, C. A. Bronkhorst, N. N. Carlson, C. K. Newman, T. Haut, J. Bakosi, J. W. Gibbs, V. Livescu, S. A. Vander Wiel, A. J. Clarke, M. W. Schraad, T. Blacker, H. Lim, T. Rodgers, S. Owen, F. Abdeljawad, J. Madison, A. T. Anderson, J.-L. Fattebert, R. M. Ferencz, N. E. Hodge, S. A. Khairallah, and O. Walton, "Modeling of additive manufacturing processes for metals: Challenges and opportunities," *Current Opinion in Solid State and Materials Science*, vol. 21, no. 4, pp. 198–206, 2017.

[3] A. Rai, H. Helmer, and C. Körner, "Simulation of grain structure evolution during powder bed based additive manufacturing," *Additive Manufacturing*, vol. 13, pp. 124–134, 2017.

[4] D. Anand and D. R. Kumar, "Effect of thickness and grain size on flow stress of very thin brass sheets," *Procedia Materials Science*, vol. 6, pp. 154–160, 2014.

[5] S. Miyazaki, K. Shibata, and H. Fujita, "Effect of specimen thickness on mechanical properties of polycrystalline aggregates with various grain sizes," *Acta Metallurgica*, vol. 27, pp. 855–862, 1979.

[6] M. G. D. Geers, W. A. M. Brekelmans, and P. J. M. Janssen, "Size effects in miniaturized polycrystalline FCC samples: Strengthening versus weakening," *International Journal of Solids and Structures*, vol. 43, no. 24, pp. 7304–7321, 2006.

[7] Y. Zhang, L. Wu, X. Guo, S. Kane, Y. Deng, Y. Jung, J. Lee, and J. Zhang, "Additive Manufacturing of Metallic Materials: A Review," *Journal of Materials Engineering and Performance*, vol. 27, pp. 1–13, 2018.

[8] J. J. Lewandowskiand and M. Seifi, “Metal additive manufacturing: A review of mechanical properties,” *Annual Review of Materials Research*, vol. 46, no. 1, pp. 151–186, 2016.

[9] S. A. M. Tofail, E. P. Koumoulos, A. Bandyopadhyay, S. Bose, L. O’Donoghue, and C. Charitidis, “Additive manufacturing: scientific and technological challenges, market uptake and opportunities,” *Materials Today*, vol. 21, no. 1, pp. 22–37, 2018.

[10] O. Abdulhameed, A. Al-Ahmari, W. Ameen, and S. H. Mian, “Additive manufacturing: Challenges, trends, and applications,” *Advances in Mechanical Engineering*, vol. 11, no. 2, pp. 1–27, 2019.

[11] R. Singh, A. Gupta, O. Tripathi, S. Srivastava, B. Singh, A. Awasthi, S. K. Rajput, P. Sonia, P. Singhal, and K. K. Saxena, “Powder bed fusion process in additive manufacturing: An overview,” *Materials Today: Proceedings*, vol. 26, pp. 3058–3070, 2020.

[12] K. Kempen, L. Thijs, E. Yasa, M. Badrossamay, W. Verheecke, and J. P. Kruth, “Process optimization and microstructural analysis for selective laser melting of AlSi10Mg,” 08 2011.

[13] W. J. Sames, F. A. List, S. Pannala, R. R. Dehoff, and S. S. Babu, “The metallurgy and processing science of metal additive manufacturing,” *International Materials Reviews*, vol. 61, no. 5, pp. 315–360, 2016.

[14] M. Jamshidinia, “Numerical modeling of heat distribution in the electron beam melting of Ti-6Al-4V,” *Journal of Manufacturing Science and Engineering*, vol. 135, pp. 061010–1, 2013.

[15] J. Holm, N., N. Hassold, G., and A. Miodownik, M., “On misorientation distribution evolution during anisotropic grain growth,” *Acta Materialia*, vol. 49, p. 2981–2991, 2001.

[16] Y. Kok, X. P. Tan, P. Wang, M. L. S. Nai, N. H. Loh, E. Liu, and S. B. Tor, “Anisotropy and heterogeneity of microstructure and mechanical properties in metal additive manufacturing: A critical review,” *Materials & Design*, vol. 139, pp. 565–586, 2018.

[17] K. N. Amato, S. M. Gaytan, L. E. Murr, E. Martinez, P. W. Shindo, J. Hernandez, S. Collins, and F. Medina, "Microstructures and mechanical behavior of inconel 718 fabricated by selective laser melting," *Acta Materialia*, vol. 60, no. 5, pp. 2229–2239, 2012.

[18] Z. Wang, K. Guan, M. Gao, X. Li, X. Chen, and X. Zeng, "The microstructure and mechanical properties of deposited-IN718 by selective laser melting," *Journal of Alloys and Compounds*, vol. 513, p. 518–523, 2012.

[19] E. Hovig, A. Azar, F. Grytten, K. Sørby, and E. Andreassen, "Determination of Anisotropic Mechanical Properties for Materials Processed by Laser Powder Bed Fusion," *Advances in Materials Science and Engineering*, vol. 2018, pp. 1–20, 2018.

[20] L. Thijs, F. Verhaeghe, T. Craeghs, J. Humbeeck, and J. P. Kruth, "A study of the microstructural evolution during selective laser melting of Ti–6Al–4V," *Acta Materialia*, vol. 58, pp. 3303–3312, 2010.

[21] T. Ishimoto, K. Hagihara, K. Hisamoto, S. H. Sun, and T. Nakano, "Crystallographic texture control of beta-type Ti–15Mo–5Zr–3Al alloy by selective laser melting for the development of novel implants with a biocompatible low Young's modulus," *Scripta Materialia*, vol. 132, pp. 34–38, 2017.

[22] T. Ishimoto, K. Hagihara, K. Hisamoto, and T. Nakano, "Stability of crystallographic texture in laser powder bed fusion: Understanding the competition of crystal growth using a single crystalline seed," *Additive Manufacturing*, vol. 43, p. 102004, 2021.

[23] A. Charmi, R. Falkenberg, L. Àvila, G. Mohr, K. Sommer, A. Ulbricht, M. Sprengel, R. Neumann, B. Skrotzki, and A. Evans, "Mechanical anisotropy of additively manufactured stainless steel 316L: An experimental and numerical study," *Materials Science and Engineering: A*, vol. 799, p. 140154, 2021.

[24] M. Guden, H. Yavaş, A. A. Tanrikulu, A. Tasdemirci, B. Akın, S. Enser, A. Karakuş, and B. A. Hamat, "Orientation dependent tensile properties of a selective-laser-melt 316L stainless steel," *Materials Science and Engineering: A*, vol. 824, p. 141808, 2021.

[25] A. Lopes, F. Barlat, J. Gracio, J. Duarte, and E. Rauch, "Effect of texture and microstructure on strain hardening anisotropy for aluminum deformed in uniaxial tension and simple shear," *International Journal of Plasticity*, vol. 19, pp. 1–22, 2003.

[26] S. Dumoulin, O. Engler, O. S. Hopperstad, and O. G. Lademo, "Description of plastic anisotropy in AA6063-T6 using the crystal plasticity finite element method," *Modelling and Simulation in Materials Science and Engineering*, vol. 20, p. 055008, 2012.

[27] W. Frazier, "Metal Additive Manufacturing: A Review," *Journal of Materials Engineering and Performance*, vol. 23, pp. 1917–1928, 2014.

[28] K. Zhang, B. Holmedal, O. S. Hopperstad, S. Dumoulin, J. Gawad, A. Van Bael, and P. Van Houtte, "Multi-level Modelling of Mechanical Anisotropy of Commercial Pure Aluminium Plate: Crystal Plasticity Models, Advanced Yield Functions and Parameter Identification," *International Journal of Plasticity*, vol. 66, pp. 3–30, 2015.

[29] T. Yalçinkaya, İ. Özdemir, and I. Simonovski, "Micromechanical modeling of intrinsic and specimen size effects in microforming.," *International Journal of Material Forming*, vol. 11, pp. 729–741, 2018.

[30] E. Hall, "The Deformation and Ageing of Mild Steel: III Discussion of Results," *Proc. Phys. Soc.*, vol. 643, pp. 747–753, 1951.

[31] P. J. M. Janssen, T. H. de Keijser, and M. G. D. Geers, "An experimental assessment of grain size effects in the uniaxial straining of thin al sheet with a few grains across the thickness," *Materials Science and Engineering: A*, vol. 419, pp. 238–248, 2006.

[32] H. Kim and Y. Lee, "Size dependence of flow stress and plastic behaviour in microforming of polycrystalline metallic materials," *Proceedings of the Institution of Mechanical Engineers, Part C: Journal of Mechanical Engineering Science*, vol. 226, pp. 403–412, 2012.

[33] E. Hug and C. Keller, "Intrinsic Effects due to the Reduction of Thickness on

the Mechanical Behavior of Nickel Polycrystals," *Metallurgical and Materials Transactions: A*, vol. 41, pp. 2498–2506, 2010.

[34] C. Keller, E. Hug, and F. Xavier, "Microstructural size effects on mechanical properties of high purity nickel," *International Journal of Plasticity*, vol. 27, pp. 635–654, 2011.

[35] A. Kals, T. and R. Eckstein, "Miniaturization in sheet metal working," *Journal of Materials Processing Technology*, vol. 103, pp. 95–101, 2000.

[36] L. V. Raulea, A. M. Goijaerts, L. E. Govaert, and F. P. T. Baaijens, "Size effects in the processing of thin metal sheets," *Journal of Materials Processing Technology*, vol. 115, pp. 44–48, 2001.

[37] C. Keller, E. Hug, R. Retoux, and F. Xavier, "TEM study of dislocation patterns in near-surface and core regions of deformed nickel polycrystals with few grains across the cross section," *Mechanics of Materials*, vol. 42, pp. 44–54, 2010.

[38] O. Bulut, S. S. Acar, and T. Yalçinkaya, "The influence of thickness/grain size ratio in microforming through crystal plasticity," *Procedia Structural Integrity*, vol. 35, pp. 228–236, 2022.

[39] Y. Huang, "A user-material subroutine incroporating single crystal plasticity in the abaqus finite element program," *Mech Report*, vol. 178, 1991.

[40] G. I. Taylor, "Plastic strain in metals," *Journal of the Institute of Metals*, vol. 62, pp. 307–324, 1938.

[41] R. Hill, "Generalized constitutive relations for incremental deformation of metal crystals by multislip," *Journal of the Mechanics and Physics of Solids*, vol. 14, no. 2, pp. 95–102, 1966.

[42] J. R. Rice, "Inelastic constitutive relations for solids: An internal-variable theory and its application to metal plasticity," *Journal of the Mechanics and Physics of Solids*, vol. 19, no. 6, pp. 433–455, 1971.

[43] R. Hill and J. R. Rice, "Constitutive analysis of elastic-plastic crystals at arbitrary strain," *Journal of the Mechanics and Physics of Solids*, vol. 20, no. 6, pp. 401–413, 1972.

[44] J. R. Rice, "On the structure of stress-strain relations for time-dependent plastic deformation in metals," *Journal of Applied Mechanics*, vol. 37, no. 3, pp. 728–737, 1970.

[45] R. J. Asaro, "Micromechanics of crystals and polycrystals," vol. 23 of *Advances in Applied Mechanics*, pp. 1–115, 1983.

[46] D. Hull and D. J. Bacon, *Introduction to Dislocations*. Butterworth-Heinemann, 2001.

[47] F. Dunne and N. Petrinic, *Introduction to Computational Plasticity*. OUP Oxford, 2005.

[48] V. A. Lubarda, "Constitutive theories based on the multiplicative decomposition of deformation gradient: Thermoelasticity, elastoplasticity, and biomechanics," *Applied Mechanics Reviews*, vol. 57, no. 2, pp. 95–108, 2004.

[49] J. C. Simo and T. J. R. Hughes, *Computational Inelasticity*. Springer, New York, NY, 1998.

[50] J. W. Hutchinson, "Bounds and self-consistent estimates for creep of polycrystalline materials," *Proceedings of the Royal Society of London. Series A, Mathematical and Physical Sciences*, vol. 348, no. 1652, pp. 101–127, 1976.

[51] D. Peirce, R. J. Asaro, and A. Needleman, "An analysis of nonuniform and localized deformation in ductile single crystals," *Acta Metallurgica*, vol. 30, pp. 1087–1119, 1982.

[52] U. F. Kocks, C. N. Tomé, and H. R. Wenk, *Texture and Anisotropy. Preferred Orientations in Polycrystals and Their Effect on Material Properties*. 2000.

[53] R. Becker and S. Panchanadeeswaran, "Crystal rotations represented as rodrigues vectors," *Textures and Microstructures*, vol. 10, pp. 167–194, 1988.

[54] Ö. Kahveci, C. Gençoğlu, and T. Yalçinkaya, "Experimental analysis and multiscale modeling of the dynamics of a fiber-optic coil," *Sensors*, vol. 22, p. 582, 2022.

[55] T. Yalçinkaya, S. O. Çakmak, and C. Tekoğlu, “A crystal plasticity based finite element framework for RVE calculations of two-phase materials: Void nucleation in dual-phase steels,” *Finite Elements in Analysis and Design*, vol. 187, p. 103510, 2021.

[56] R. Quey, P. Dawson, and F. Barbe, “Large-scale 3D random polycrystals for the finite element method: Generation, meshing and remeshing,” *Computer Methods in Applied Mechanics and Engineering*, vol. 200, pp. 1729–1745, 2011.

[57] K. Hitti, P. Laure, T. Coupez, L. Silva, and M. Bernacki, “Precise generation of complex statistical representative volume elements (rves) in a finite element context,” *Computational Materials Science*, vol. 61, pp. 224–238, 2012.

[58] G. Mollon and J. Zhao, “Fourier–voronoi-based generation of realistic samples for discrete modelling of granular materials,” *Granular Matter*, vol. 14, p. 621–638, 2012.

[59] W. X. Xu and H. S. Chen, “Numerical investigation of effect of particle shape and particle size distribution on fresh cement paste microstructure via random sequential packing of dodecahedral cement particles,” *Computers & Structures*, vol. 114-115, pp. 35–45, 2013.

[60] S. S. Acar, O. Bulut, and T. Yalçinkaya, “Crystal plasticity modeling of additively manufactured metallic microstructures,” *Procedia Structural Integrity*, vol. 35, pp. 219–227, 2022.

[61] C. Tekoğlu, “Representative volume element calculations under constant stress triaxiality, lode parameter, and shear ratio,” *International Journal of Solids and Structures*, vol. 51, pp. 4544–4553, 12 2014.

[62] T. Kanit, S. Forest, I. Galliet, V. Mounoury, and D. Jeulin, “Determination of the size of the representative volume element for random composites: statistical and numerical approach,” *International Journal of Solids and Structures*, vol. 40, no. 13, pp. 3647–3679, 2003.

[63] S. Nezamabadi, M. Potier-Ferry, H. Zahrouni, and J. Yvonnet, “Compressive failure of composites: A computational homogenization approach,” *Composite Structures*, vol. 127, pp. 60–68, 2015.

[64] H. Granum, V. Aune, T. Børvik, and O. S. Hopperstad, "Effect of heat-treatment on the structural response of blast-loaded aluminium plates with pre-cut slits," *International Journal of Impact Engineering*, p. 103306, 2019.

[65] E. Nakamachi, C. L. Xie, H. Morimoto, K. Morita, and N. Yokoyama, "Formability assessment of FCC aluminum alloy sheet by using elastic/crystalline viscoplastic finite element analysis," *International Journal of Plasticity*, vol. 18, pp. 617–632, 10 2002.

[66] W. Liu, B. Chen, and Y. Pang, "Numerical investigation of evolution of earing, anisotropic yield and plastic potentials in cold rolled fcc aluminium alloy based on the crystallographic texture measurements," *European Journal of Mechanics - A/Solids*, vol. 75, pp. 41–55, 12 2019.

[67] T. Yalçinkaya, "Strain gradient crystal plasticity: Thermodynamics and implementation.," *Handbook of Nonlocal Continuum Mechanics for Materials and Structures*, pp. 1001–1033, 2019.

[68] T. Yalçinkaya, İ. Özdemir, and İ. T. Tandoğan, "Misorientation and grain boundary orientation dependent grain boundary response in polycrystalline plasticity," *Computational Mechanics*, vol. 67, p. 937–954, 2021.

[69] T. Yalçinkaya, İ. T. Tandoğan, and İ. Özdemir, "Void growth based intergranular ductile fracture in strain gradient polycrystalline plasticity," *International Journal of Plasticity*, vol. 147, p. 103123, 2021.

[70] Z. Yuan, Y. Tu, T. Yuan, Y. Zhang, and Y. Huang, "Size effects on mechanical properties of pure industrial aluminum sheet for micro/meso scale plastic deformation: Experiment and modeling," *Journal of Alloys and Compounds*, vol. 859, p. 157752, 11 2020.

[71] T. Yalçinkaya, İ. Özdemir, and A. O. Firat, "Inter-granular cracking through strain gradient crystal plasticity and cohesive zone modeling approaches," *Theoretical and Applied Fracture Mechanics*, vol. 103, p. 102306, 2019.

[72] C. Mondal, A. Singh, A. K. Mukhopadhyay, and K. Chattopadhyay, "Effects of different modes of hot cross-rolling in 7010 aluminum alloy: Part ii. mechani-

cal properties anisotropy," *Metallurgical and Materials Transactions A*, vol. 44, p. 2764, 2013.